



CARRIER DYNAMICS IN MID-INFRARED QUANTUM
WELL LASERS USING TIME-RESOLVED
PHOTOLUMINESCENCE

THESIS

Steven M Gorski, Capt, USAF

AFIT/GAP/ENP/02M-01

DEPARTMENT OF THE AIR FORCE
AIR UNIVERSITY

AIR FORCE INSTITUTE OF TECHNOLOGY

Wright-Patterson Air Force Base, Ohio

APPROVED FOR PUBLIC RELEASE; DISTRIBUTION UNLIMITED.

Report Documentation Page

Report Date 4 Mar 02	Report Type Final	Dates Covered (from... to) -
Title and Subtitle Carrier Dynamics In Mid-Infrared Quantum Well Lasers Using Time-Resolved Photoluminescence	Contract Number	
	Grant Number	
	Program Element Number	
Author(s) Capt Steven M. Gorski, USAF	Project Number	
	Task Number	
	Work Unit Number	
Performing Organization Name(s) and Address(es) Air Force Institute of Technology Graduate School of Engineering (AFIT/EN) 2950 P Street, Bldg 640 WPAFB OH 45433-7765	Performing Organization Report Number AFIT/GAP/ENP/02M-01	
Sponsoring/Monitoring Agency Name(s) and Address(es) Air Force Reserach Laboratory Directed Enegy Directorate ATTN: Ms. Sylvia Doranto Kirtland AFB, NM 87117	Sponsor/Monitor's Acronym(s)	
	Sponsor/Monitor's Report Number(s)	
Distribution/Availability Statement Approved for public release, distribution unlimited		
Supplementary Notes The original document contains color images.		
Abstract Research in mid-infrared laser technology has uncovered numerous applications for commercial and government use. A limiting factor for mid-infrared semiconductors is nonradiative recombination, which is a process that produces excess heat without emitting a photon. Nonradiative recombination mechanisms occur over a short time period and difficult to measure. Growth methods have significantly reduced the nonradiative recombination in some materials. The objective of this research is to further the understanding of how quantum well structures impact carrier recombination. In AsSb/InAlSb and InAs/GaSb quantum well structures were studied with time-resolved photoluminescence utilizing upconversion, a non-linear wave mixing technique. This research reports Shockley-Read-Hall, radiative, and Auger recombination coefficients at 77k. The luminescence rise times of type I and type II structures are also compared. The number of states available within the quantum well was found to dictate how quickly carriers were able to recombine radiatively. Finally, spectral data was taken to examine the spectral decay of the luminescence. Carrier temperatures were extracted from the spectral data. Type I structures were found to have hotter carrier temperatures and higher Auger coefficients than type II structures.		

Subject Terms Time resolved photoluminescence, Sum frequency generation, upconversion, quantum well lasers. Gallium Indium Antimonide, Indium Arsenide, Indium Aluminum Arsenide Antimonide, carrier relaxation time, photoluminescence spectra, Auger recombination	
Report Classification unclassified	Classification of this page unclassified
Classification of Abstract unclassified	Limitation of Abstract UU
Number of Pages 92	

The views expressed in this thesis are those of the author and do not reflect the official policy or position of the United States Air Force, Department of Defense, or the U.S. Government.

AFIT/GAP/ENP/02M-01

CARRIER DYNAMICS IN MID-INFRARED QUANTUM WELL LASERS USING
TIME-RESOLVED PHOTOLUMINESCENCE

THESIS

Presented to the Faculty of the Graduate School of Engineering and Management

of the Air Force Institute of Technology

Air University

Air Education and Training Command

In Partial Fulfillment of the Requirements for the

Degree of Master of Science in Applied Physics

Steven M Gorski, BS

Captain, USAF

March 2002

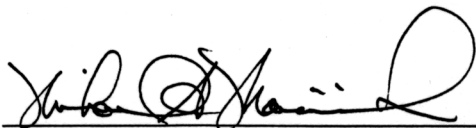
APPROVED FOR PUBLIC RELEASE; DISTRIBUTION UNLIMITED

AFIT/GAP/ENP/02M-01

CARRIER DYNAMICS IN MID-INFRARED QUANTUM WELL LASERS USING
TIME-RESOLVED PHOTOLUMINESCENCE


Steven M. Gorski, BS
Capt, USAF

Approved:



Lt Col Michael A. Marciniak, Advisor

5 Mar 02
date



Dr. Robert L. Hengehold, Member

5 Mar 02
date



Dr. David E. Weeks, Member

5 Mar 02
date

Acknowledgments

This project was the greatest challenge I've had to face in my academic career, and there are a number of people that made this possible that I would like to thank here. Greg Smith and Rick Patton always took time to answer my technical questions, and they gave me important tips on how to avoid bodily harm while in the lab. LtCol Michael Marciniak took endless hours out of his day to discuss solutions to the many roadblocks I encountered on the way. He shared in my frustration and gave me encouragement when I needed it. In addition, my thanks go out to the service men and women that were getting the mission done while I took a break to go to school.

I would also like to thank Richard Silski. He taught me it was better to understand how things worked rather than just taking someone's word that it did. From Chess strategy to replacing alternators, he taught me many things, and is certainly the reason why I am a physicist today.

Most importantly, I would like to thank my wife. Without her I would not have the opportunity to be here. More than once she gave me the motivation to press on when I felt like I'd had enough. In the process I think she learned a little more physics than she cares to admit. Thank you for your undying support and your unbelievable patience.

Steven M. Gorski

Table of Contents

	Page
Acknowledgements	iv
List of Figures	viii
List of Tables.....	xi
Abstract	xii
1. Introduction	1
1.1. Motivation	1
1.2. Background	4
1.3. Approach	5
1.4. Overview	6
2. Theory	7
2.1. Density of States.....	7
2.2. Carrier Distribution Function.....	9
2.3. Recombination Mechanisms	11
2.4. Carrier Scattering	13
3. Experiment	15
3.1. Upconversion Theory	16
3.2. Experimental Set Up	19
3.2.1. Laser Source.....	19
3.2.2. Optical Path.....	23
3.2.2.1. PL Path.....	23
3.2.2.2. Pump Beam Path	24

3.2.2.3. Beam Overlap.....	24
3.2.4. Signal Collection.....	25
3.2.4.1. Photoluminescence Experiment.....	25
3.2.4.2. TRPL Experiment	26
3.3. Upconversion Efficiency.....	28
3.4. Sample Description	30
4. Data Analysis and Results.....	34
4.1. Determining Recombination Coefficients.....	34
4.1.1. Analysis of Decay Curve.....	35
4.1.2. Recombination Coefficient Results.....	44
4.2. Carrier Relaxation	46
4.3. Carrier Temperature	51
4.3.1. Carrier Temperature Results	51
4.3.2. Carrier Temperature Modeling.....	55
5. Conclusion.....	60
5.1. Summary	60
5.2. Future Work	61
Appendix A. Mathcad Program	63
Appendix A.1. Crystal Rotation Angle	63
Appendix A.2. Finding the Phase Mismatch.....	66
Appendix A.3. Carrier temperature.....	68
Appendix B. Experimental Data	70

Appendix B.1. Decay Curves.....	70
Appendix B.2. Rise Time Experimental Data.....	72
Appendix B.3. Rise Time Curve Fits	74
Bibliography.....	75

List of Figures

Figure	Page
Figure 1.1. Aircraft losses due to IR missiles in several conflicts. During Operation Allied Force in Kosovo, RF missiles downed two aircraft, IR missiles struck two aircraft, and AAA damaged two aircraft (Kent, 2000 and Lambeth, 2001)	2
Figure 1.2. Laser IR countermeasure systems. (a) Advanced Tactical IRCM System developed by Sanders. The insert shows the rotating mount that houses the laser source (Sanders, 2000). (b) Laser designed for IRCM with reduced size for fighter applications (Goyal <i>et al.</i> , 2000)	3
Figure 2.1. Density of States in a quantum well and bulk material. The dashed line represents a 3-D free particle, while the solid line represents a 3-D particle confined to a 1-D quantum well. E_a and E_b are the energy gaps associated with the materials that make up the barriers and well. E_1 and E_2 represent the first two confined energy states in the well of width L (Saleh and Teich, 1991:571)	9
Figure 2.2. Example PL curve. Low energy side is governed by density of states function. High-energy tail is due to carrier distribution function. The band tailing effect is shown as energy states available below the band-gap energy E_g	10
Figure 2.3. Valence band Auger process (CHSH). An electron-hole pair recombines and the resulting energy promotes a hole from the split-off band to the heavy-hole band. In mid-IR semiconductors, $E_g \approx \Delta$ making the CHSH process dominate at high carrier densities (Haug, 1988)	12
Figure 3.1. Wave mixing resulting in the time resolution of the luminescence. a) Depicts the luminescence curve over time. b) Represents the pump beam at some delay time τ	16
Figure 3.2. Phase matching geometry required for upconversion. The pump beam and PL beam enter the crystal at 20°	18
Figure 3.3. Experimental set up in TRPL experiment. The Ti:Sapphire laser creates a 122 fs pulse that is split into two paths. The PL beam travels through a delay stage before exciting the sample. Luminescence is collected and mixed with the pump beam in the KTA crystal. The upconverted beam is then directed to the spectrometer and photon counter (Cooley, 1997)	20

Figure	Page
Figure 3.4. a) Temporal pulse width of Ti:Sapphire laser. FWHM is measured to be $\Delta t_m = 188$ fs. A correction factor of 0.648 is applied to obtain an actual pulse width of $\Delta t_a = 122$ fs b) Spectral width of Ti:Sapphire pulse with a FWHM of 10 nm.....	21
Figure 3.5. Upconversion efficiency compared to peak efficiency over the luminescence spectra of Sample 91. The Sample 91 PL curve peaks at 3.5 μm s with a FWHM indicated by the dashed lines in the figure.....	31
Figure 3.6. Sample B quantum well structure. Energy diagram with offset bands and excitation energy drawn to scale. Well and Barrier widths are also included (Cooley, 1997).....	32
Figure 3.7. Sample 88, 90, and 91 quantum well structure. Energy diagram with offset bands and excitation energy drawn to scale. Well and Barrier widths are also included (Jang and Flatte, 1998).....	33
Figure 3.8. Photoluminescence curves for each sample tested. Sample B is a type I structure Sample 88, 90, and 91 are type II. Intensities shown as true scale.	33
Figure 4.1. Sample TRPL data collected. The intensity of the upconverted signal from an optically excited quantum well structure is plotted over 3 nanoseconds. Multiple curves indicate varying excitation power.....	36
Figure 4.2. Carrier density as a function of Luminescence intensity. Data points are the initial ($t = 0$) carrier densities generated by the laser pulse, which were calculated using Eq(4.4). The solid line represents a fitting function found in Eq (4.5) used to related carrier densities at $t > 0$ to luminescence intensities.....	40
Figure 4.3. Curve fit to estimate A_{SRH} . SRH recombination is assumed to dominate after 2.5 ns. A_{SRH} is determined by fitting an exponential decay curve to the data.....	42
Figure 4.4. Error surface resulting from the fit of Eq (4.1) to the experimental data as a function of B_{rad} and C_{Auger} . The minimum point on this surface represents the best fit for a given A_{SRH} and initial carrier density.....	43
Figure 4.5. Error surface resulting from the fit of Eq (4.1) to the experimental data as a function of A_{SRH} and initial carrier density. The minimum point on this surface represents the best fit of the experimental data.....	44
Figure 4.6. Carrier density decay over 3-ns time period for various excitation powers	46

Figure	Page
Figure 4.7. Luminescence rise time for Sample 91 at various excitation powers. Data was recorded at 2-ps intervals. Zero on the time scale represents the arrival of the excitation pulse.....	47
Figure 4.8. Example fit to the normalized rise data with $R^2 = 0.97$	49
Figure 4.9. Carrier Density rise time for a) Sample 91 at multiple excitation powers, and b) for each sample. Rise time increases with carrier density and decreases with well width for the Type II structures.....	50
Figure 4.10. Spectral data for Sample 91 at different decay times in terms of upconverted energy. The high-energy tail is fit with an exponential function to determine carrier temperature.....	52
Figure 4.11. Gaussian curve fits to the low energy side of the spectral data. The empirical parameter E_0 listed describes the density of states, and was found to vary by less than 10% over the series of spectra.....	53
Figure 4.12. Boltzmann distribution curve's used to extract carrier temperature. Average carrier temperature's cool as relax to the band edge and recombine	54
Figure 4.13. Calculated energy-loss rate as a function of carrier temperature for InAs. At low temperatures, acoustic phonons dominate resulting in higher loss rates below 40 K, which is not depicted in this figure.	56
Figure 4.14. Carrier temperature as a function of time for Sample 91 and Sample B. The theoretical model for carrier temperatures in InAs is plotted as a solid line. An initial temperature of 350 K and a fitting parameter $C = 0.5$ was used to fit the data.....	58

List of Tables

Table	Page
Table 4.1. Analysis of the error in unknown parameters used to calculate carrier density....	39
Table 4.2. Experimentally determined recombination coefficients for each sample.	45
Table 4.3. Calculated rise time for each sample at various excitation powers. Rise time is measured from the 10%-90% intensity points.....	48

Abstract

The objective of this research is to improve the performance of semiconductor quantum well lasers operating in the mid-infrared. Research in mid-infrared laser technology has uncovered numerous applications for commercial and government use. Many military applications require operation near room temperature with compact power supplies. Limiting factors for improving the efficiency of mid-infrared semiconductor lasers at elevated temperatures include non-radiative recombination and carrier relaxation. Carrier lifetimes are typically on the order of 5 nsec, therefore, recombination mechanisms and carrier relaxation times are difficult to measure directly. Time-resolved photoluminescence (TRPL), utilizing a non-linear wave mixing technique known as upconversion, is used to study the time evolution of carrier densities in semiconductor lasers. Carrier recombination and relaxation information is extracted from this data to further the understanding of how quantum well structures impact semiconductor laser performance.

InAsSb/InAlSb type I and InAs/GaInSb type II multiple quantum well structures were studied. Auger recombination coefficients were determined to be $3.3 \pm 0.1 \times 10^{-31} \text{ cm}^6/\text{s}$ for type I structures and $6.0 \pm 1.0 \times 10^{-32} \text{ cm}^6/\text{s}$ for type II structures at 77 K. The Auger coefficient, which describes a non-radiative process that can dominate when using wavelengths in the mid-IR, was found to be higher in type I than type II structures. This trend is in agreement with previous research, however, there has been a wide range of reported values for the Auger coefficient in similar material. Therefore, careful data reduction and error analysis is included to bound the recombination coefficients with some degree of certainty. Carrier temperatures were extracted from the spectral TRPL data.

Type I structures were found to have hotter carrier temperatures than type II structures, which is consistent with the Auger coefficient results.

TRPL data was also used to investigate carrier relaxation, or the time required for energetic carrier will cool to the bottom of a quantum well, where it can recombine radiatively. The carrier relaxation times were found to increase with excitation power and decrease as the quantum well width increased. Carrier relaxation times for the type II structures were 16, 8, and 5 ps for InAs wells of width 20, 23, and 26, respectively. These relaxation times were measured at 300 mW excitation power with a fixed GaInSb well width of 24 Angstroms.

CARRIER DYNAMICS IN MID-INFRARED QUANTUM WELL LASERS USING TIME-RESOLVED PHOTOLUMINESCENCE

1. Introduction

Mid-infrared (IR) semiconductor lasers are well suited for a variety of applications including pollution monitoring, optical communications, and laser surgical equipment. The Air Force is particularly interested in applying this technology to IR counter-measures and laser radar. IR guided missiles are abundant and proliferated worldwide, and IR passive detection systems are being incorporated into many fourth generation aircraft. Antimony based semiconductors are a good choice for IR laser devices because of their flexibility to be grown to take advantage of the atmospheric transmission window from 3-5 μm . While the size of such devices is attractive for aircraft applications, the efficiency has been marginal. This paper will focus on two processes, carrier recombination and carrier relaxation, that have a significant effect on the performance mid-IR semiconductor devices.

1.1. Motivation

There are over 500,000 IR guided missiles proliferated worldwide that pose a significant threat to allied aircraft (Sawyer, 2000). To illustrate this threat, Figure 1.1 shows the number of aircraft that have been lost to IR missiles in several conflicts dating back to 1950's. Man Portable Air Defense Systems (MANPADS) are IR weapons of particular concern to mission planners because of their mobility. Avoidance has been the

primary tactic to defeat the MANPAD threat in recent conflicts. In Operations ALLIED FORCE and ENDURING FREEDOM, combat aircraft in hostile territory were flown above 15,000 ft with few exceptions (Lambeth, 2001). Airdrops and visual target identification become difficult at this altitude, and operators are further restricted by weather constraints. Unfortunately, avoidance may not be a plausible tactic. When operating out of foreign airfields, aircraft pass through the heart of the MANPAD engagement envelopes on take-off and landing. In an effort to counter the IR threat, the Air Force has researched a number of laser based IR countermeasures (IRCM).

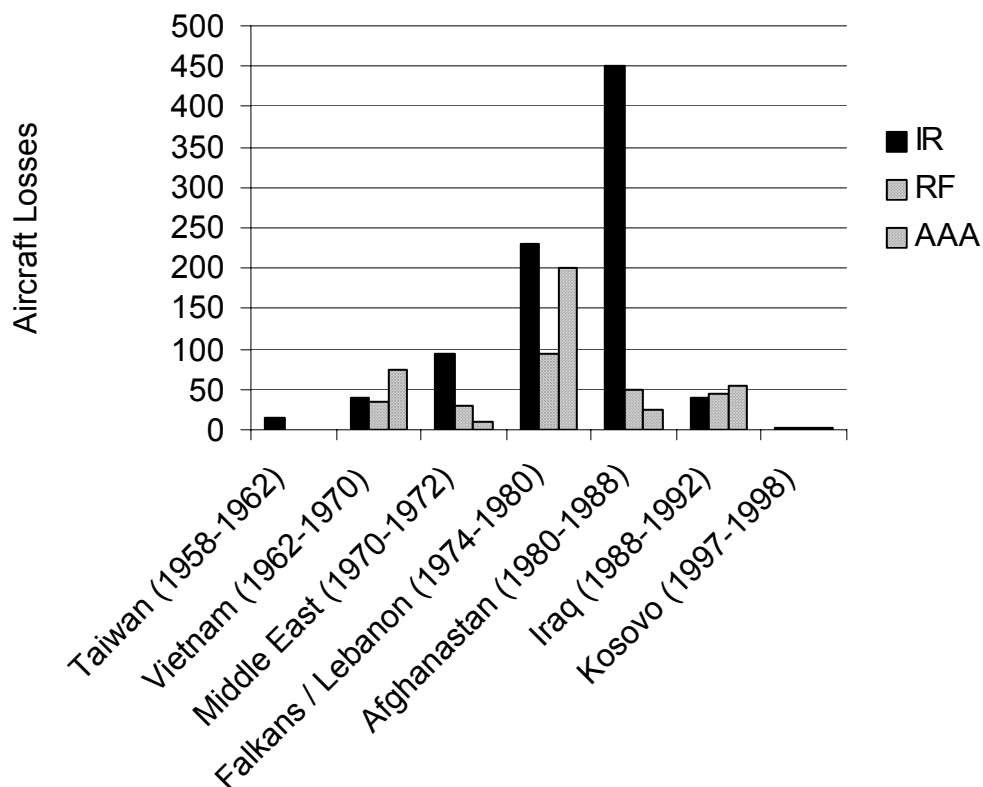


Figure 1.1. Aircraft losses due to IR missiles in several conflicts. During Operation Allied Force in Kosovo, RF missiles downed two aircraft, IR missiles struck two aircraft, and AAA damaged two aircraft (Kent, 2000 and Lambeth, 2001).

The Sensors Directorate of the Air Force Research Laboratory established the Laser Infrared Flyout Experiment (LIFE) program to test advanced IRCM protection of large aircraft (Taylor, 2001). Figure 1.2 (a) shows one of the prototypes for the LIFE program developed by Sanders (Sanders, 2000). A large aircraft would carry up to four laser IRCM systems to provide all-aspect protection. Fighter aircraft, however, lack the space and power required to operate these countermeasures. Further research is being conducted to reduce the size and improve the efficiency of laser countermeasures to field an IRCM system for fighter aircraft. Figure 1.2 (b) shows a semiconductor laser designed to achieve that goal.

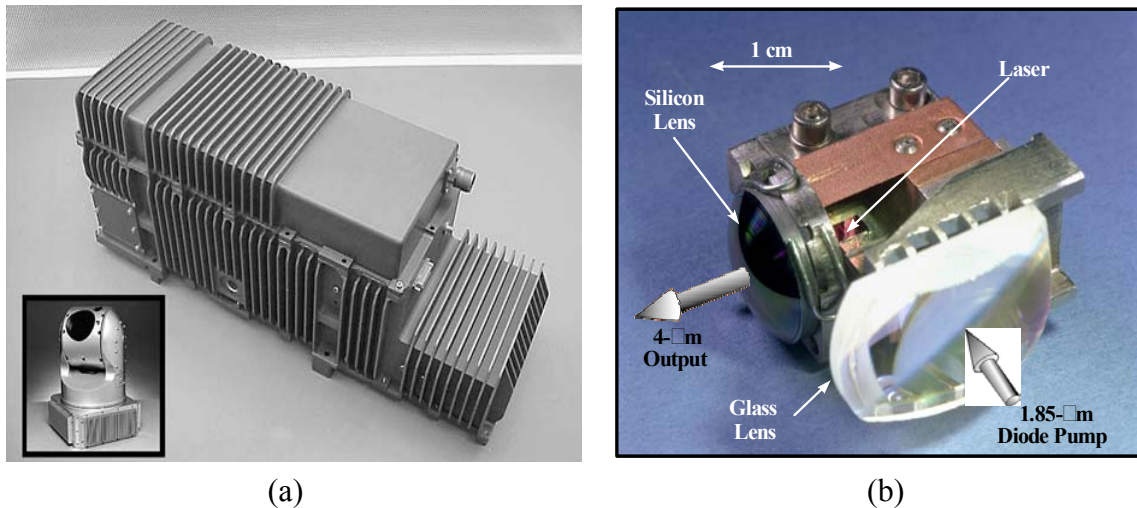


Figure 1.2. Laser IR countermeasure systems. (a) Advanced Tactical IRCM System developed by Sanders. The insert shows the rotating mount that houses the laser source (Sanders, 2000). (b) Laser designed for IRCM with reduced size for fighter applications (Goyal *et al.*, 2000).

1.2. Background

Efforts to grow quantum well laser structures designed to operate in the mid-IR range have focused on InAsSb type I structures (Turner, 1995; Lane *et al.*, 1997). Lane has shown that these structures require half the threshold current required for laser operation than similar heterostructure lasers (Lane *et al.*, 1997). Recently, type II structures have proven even more efficient by decreasing nonradiative recombination processes through band-gap engineering (Jang and Flatte, 1998). Carrier relaxation has been studied in type II materials as a function of excitation power (Bogges *et al.*, 2000), but the effect of varying the well width has been limited to single quantum wells (Davis *et al.*, 1994). Laser performance continues to improve as the impact of the growth process is better understood.

Time resolved photoluminescence (TRPL); first described by Mahr, is an experimental method that provides the temporal resolution necessary to study the rapid recombination of carriers in semiconductor devices (Mahr and Hirsch, 1974). The TRPL technique is used to describe the evolution of carrier densities in an excited semiconductor. Extensive work has been done at the University of Iowa to determine recombination rates in specially grown mid-IR semiconductors designed to reduce nonradiative recombination (Jang and Flatte, 1998; Jang *et al.*, 1996). Work at AFIT has been done to determine recombination rates (Cooley, 1997; McKay, 2000), and carrier densities based on spectral width (Franz, 1997). This experiment draws upon techniques and methods of analysis from previous work in an effort to further the understanding of carrier dynamics in mid-IR semiconductors.

1.3 Approach

The TRPL experiment uses frequency upconversion to study the characteristics of photoluminescence from mid-IR semiconductors. Upconversion is a method of wave mixing used to measure the luminescence, which is described in detail by Shah (Shah, 1988). Multiple methods have been developed to detect luminescence over very short time periods, including direct detection with streak cameras, photoconductive response, and pump-probe spectroscopy. Upconversion is considered the best technique for studying carrier recombination because it provides the best temporal resolution and does not require any modifications to the sample (Jang and Flatte, 1998). The TRPL experiment can be used to study the temporal and spectral aspects of the luminescence, both of which were accomplished for this paper.

The TRPL experiment describes the photon intensity over time. To extract meaningful information about the semiconductor itself, a relationship between carrier density and luminescence intensity must be determined. The initial carrier density created in the semiconductor by an excitation pulse is calculated for multiple excitation powers (Sermage, 1986). These theoretical results are then matched to experimental luminescence intensities at the same excitation power. A function is then fit to these data points to describe carrier density in terms of luminescence intensity. At this point, the recombination rate equation can be fit to the carrier density data, and the recombination coefficients can be extracted. The recombination rate equation is:

$$-\frac{dn}{dt} = A_{SRH} \cdot n + B_{rad} \cdot n^2 + C_{Auger} \cdot n^3, \quad (1.1)$$

where n is the carrier density and the A_{SRH} , B_{rad} , C_{Auger} coefficients describe the influence that a particular recombination mechanism has on the carrier density. The goal is to define these coefficients for different semiconductors to determine structural effects on device efficiency.

The initial rise of the carrier density can also be isolated to examine the carrier relaxation. The rise in the luminescence signal is a result of energetic carriers cooling to the bottom of the quantum well. The excitation energy and well width were varied to study their impact on carrier relaxation time.

The TRPL experiment can provide spectral information about the luminescence at fixed points in time. By recording data at a series of times, the spectral evolution of the luminescence can be studied. The high-energy tail of each spectrum was used to extract the effective carrier temperature. The evolution of carrier temperature provides further insight as to how quickly carriers give up energy to the lattice.

1.4 Overview

Chapter 2 will discuss the theory of carrier dynamics in a quantum well structure. Chapter 3 provides details of the TRPL experiment and the upconversion theory. The results and data analysis are described in Chapter 4. The carrier densities as a function of time for four samples will be presented. The spectral evolution of the luminescence from two samples will also be shown. Finally, Chapter 5 will discuss conclusions drawn from this analysis and recommendations for future work.

2. Theory

Quantum well (QW) structures have proved useful in increasing the efficiency of semiconductor lasers. A lower threshold current is required to create a population inversion in QW structures because they provide carrier confinement at the band edge. In addition, there is evidence that nonradiative processes are reduced in QW structures (Hausser, 1990). The benefits of a single QW structure are outweighed by the small gain medium the well creates. A series of heterojunctions with alternating band-gap energies form a multiple quantum well (MQW) structure with a much wider active region than a single quantum well. This chapter will discuss the theory that dictates the carrier dynamics in a MQW, to include carrier distributions, recombination mechanisms, and scattering. It is assumed that the reader has a basic understanding of solid-state physics and is familiar with carriers in bulk semiconductor materials.

2.1. Density of States

Epitaxial growth processes are used to create thin layers of semiconductors with varying band-gap energies. If the thickness of the narrow band-gap semiconductor is similar to or smaller than the electron de Broglie wavelength, quantum effects become important and change the properties of the semiconductor (Shah, 1996). The narrow band-gap semiconductor dictates the well width, which becomes the confined region for electrons in one dimension. The electron energy in an infinite quantum well is quantized and dependent on the well width (L) by:

$$\epsilon_a = \frac{h^2 \cdot a^2}{8 \cdot m_e \cdot L^2}, \quad (2.1)$$

where ε_a is the energy above the bottom up the conduction band, a is an integer, h is Planck's constant, and m_e is the electron effective mass. While the quantum well structures in this experiment are finite, the theory of quantized energy states still applies. The calculation of these states is complex and beyond the scope of this work. The 3-D density of states function normally applied to bulk material is no longer valid in a quantum well because carriers are now confined in one dimension. The density of states at a given energy level in the 2-D and 3-D cases is shown below (McKelvey, 1993:134,151):

$$g_{2D} = \frac{4 \cdot \pi \cdot m_e}{h^2}$$

$$g_{3D}(E) = 4 \cdot \pi \cdot \left(\frac{2 \cdot m_e}{h^2} \right)^{\frac{3}{2}} \cdot \sqrt{E} \quad (2.2)$$

The 2-D density of states is independent of energy, which is a result of the quantized energy bands. This density of states function for a quantum well is depicted in Figure 2.1 (Saleh and Teich, 1991:571). The density of states function will become perturbed at high excitation levels as a result of coulomb screening. This perturbation will cause a narrowing of the energy band-gap of a semiconductor, and radiative recombination will take place slightly below the band-gap energy. This characteristic is called band tailing and can be seen in photoluminescence curves discussed later in this chapter and experimental data.

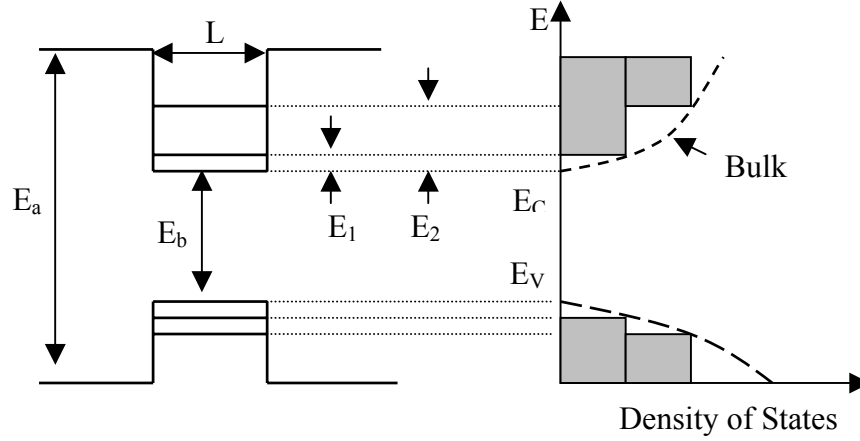


Figure 2.1. Density of States in a quantum well and bulk material. The dashed line represents a 3-D free particle, and the solid line represents a 3-D particle confined to a 1-D quantum well. E_a and E_b are the energy gaps that make up the barriers and wells. E_1 and E_2 represent the first two confined energy states in the well of width L .

2.2. Carrier Distribution Function

The density of states and the distribution of carrier energy dictate the number of carriers in a semiconductor. The Fermi-Dirac distribution function describes how carriers are spread about a single Fermi energy in an equilibrium situation. In this experiment, a non-equilibrium situation is formed when a pulsed laser creates electron-hole pairs. Two separate Fermi functions are used to describe the electron and hole distribution about quasi-Fermi energy levels. The non-equilibrium distribution functions for electrons (f_n) and holes (f_p) are:

$$f_n(E) = \frac{1}{1 + \exp\left[\frac{(E - E_{fn})}{k \cdot T}\right]}$$

$$1 - f_p(E) = \frac{1}{1 + \exp\left[\frac{(E - E_{fp})}{k \cdot T}\right]}, \quad (2.3)$$

where E_{fn} is the electron quasi-Fermi level in the conduction band, E_{fp} is the quasi-Fermi level in the valence band, and T is the carrier temperature (Bhattacharya, 1997:114). The probability of a recombination event occurring is the product of the electron and hole distribution functions. Assuming that the excitation source has been removed and the quasi-Fermi levels are deep in the bands, the carrier distribution functions can be approximated by (Saleh and Teich, 1991:584):

$$f(E) = A \cdot e^{\frac{-E}{k \cdot T}} \quad (2.4)$$

The carrier distribution and the density of states together describe the number of carriers available for recombination. This can be seen in the notional photoluminescence (PL) curve shown below in Figure 2.2.

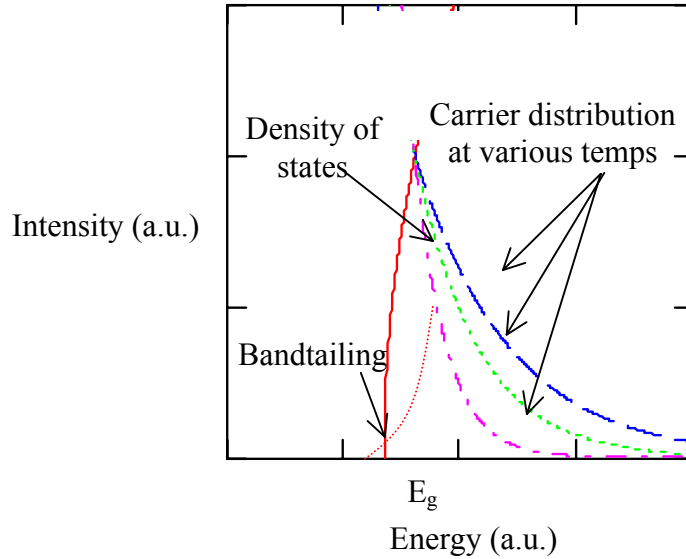


Figure 2.2. Example PL curves. Low energy side is governed by density of states function. High-energy tail is due to carrier distribution function. The band tailing effect is shown as energy states available below the band-gap energy E_g .

The density of states function dictates the low energy portion of the PL curve. The high-energy side of the curve is a result of carrier energy distribution, and will vary with temperature. As the carrier temperature decreases, the high-energy portion of a PL curve will have an increased negative slope and the width of the curve will decrease.

2.3. Recombination Mechanisms

Radiative recombination in semiconductors is measured easily and can be described by luminescence curves like the one depicted in Figure 2.2. When electron-hole pairs are created with an excitation pulse, many pairs will recombine after a certain lifetime and give off photons with energy near the band-gap of the semiconductor. Nonradiative processes are also taking place that allow electron-hole pairs to recombine without producing a photon. These nonradiative processes reduce the number of carriers that can combine radiatively, and generally produce additional heat, both of which reduce the overall efficiency of opto-electric devices. The nonradiative recombination methods that will be discussed are Shockley-Read-Hall (SRH) and Auger recombination, both of which are capable of dominating carrier recombination. The recombination rate equation that describes how the carrier density will change over time can be written as (Agrawal and Dutta, 1993):

$$-\frac{dn}{dt} = A_{SRH} \cdot n + B_{rad} \cdot n^2 + C_{Auger} \cdot n^3, \quad (2.5)$$

where n is the carrier density, A_{SRH} is the SRH coefficient, B_{rad} is the radiative coefficient, and C_{Auger} is the Auger coefficient.

SRH recombination is a single body recombination process due to a localized defect that creates energy levels deep within the band-gap of the material called a trap.

An electron can give up its energy in the form of a phonon as it recombines with a hole by way of the trap, which will heat the lattice and will not produce a photon (Coldren and Corzine, 1995:144-148). The number of traps in a semiconductor will vary with the impurities and lattice vacancies in the material. SRH recombination will be the dominant recombination process at lower carrier densities.

Unlike SRH, the Auger recombination process is a three-body process, and will therefore dominate at very high carrier concentrations. The Auger recombination occurs when the energy from an electron-hole pair recombination is transferred to another carrier through carrier-carrier interactions (Bhattacharya, 1997:147). There are multiple combinations in which Auger recombination can occur, however, the most prominent in this material is called Valence Band Auger recombination or CHSH, where C represents the conduction band, H the heavyhole band, and S the split-off band (Hausser, 1990). The CHSH Auger process, which can be seen in the schematic in Figure 2.3, dominates

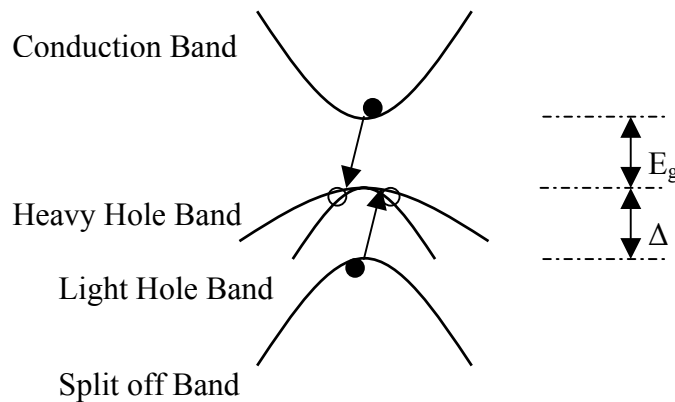


Figure 2.3. Valence band Auger process (CHSH). An electron-hole pair recombines and the resulting energy promotes a hole from the split-off band to the heavy-hole band. In mid-IR semiconductors, $E_g \approx \Delta$ making the CHSH process dominate at high carrier densities.

in this material because the band-gap energy (E_g) is nearly degenerate with the energy difference between the heavy-hole and split off bands (Δ) in the valence band structure.

Significant work has been done to find ways to suppress Auger recombination, which dominates at high carrier concentrations. Hausser *et al.* compared Auger recombination rates in bulk and QW InGaAs, and found lower Auger coefficients in QW structures (Hausser, 1990). Strain is expected to affect the Auger rate because it can alter the energy gaps, E_g and Δ . Auger recombination rates were found to vary directly with lattice temperature in InAs/GaInSb by Jang and Flatte (Jang and Flatte, 1998). The energy gaps, E_g and Δ , will vary with temperature differently, causing the Auger rate to vary with lattice temperature. The relationship between Auger recombination and carrier temperature will be discussed in Chapter 4. It is evident that the semiconductor structure and operating temperatures play a critical role in the Auger process, which greatly affect the overall efficiency of the device.

2.4. Carrier Scattering

In this experiment, a pulsed laser is used to create electron-hole pairs so that the recombination mechanisms can be studied. Electrons are excited high into the conduction band, where they interact with each other and the lattice. These highly energetic carrier interactions can negatively impact radiative recombination rates and overall device performance (Jang *et al.*, 1996). The dominant interactions that will be discussed are carrier-carrier and carrier-phonon interactions.

Carrier-carrier scattering allows for energy exchange among the highly energetic carriers created with an excitation pulse. These carriers will thermalize, or reach a

common temperature, typically within one picosecond of the excitation pulse (Shah, 1996:161). Carrier-carrier scattering dominates initially but contributes little to carrier cooling in the lattice.

The main source of energy transfer from the carriers to the lattice is through carrier-phonon scattering. Carriers will lose energy to phonons in the lattice, causing the carrier temperature to cool to the lattice temperature. Previous work has shown that highly energetic carriers in a quantum well will cool through interactions with optical phonons at carrier temperatures greater than 40 K (Yang, 1985). A MQW structure made of materials similar to the semiconductors in this experiment was found to cool by optical phonon emission on the order of 15 ps (Jang *et al.*, 1996). The cooling of energetic carriers will be investigated in this experiment and compared to other QW materials. The theory of carrier dynamics in MQW structures will be used in Chapter 4 to analyze data obtained from this experiment, and ultimately compare performance characteristics of different semiconductor samples.

3. Experiment

Luminescence emitted by mid-IR laser devices results from the recombination of electron-hole pairs excited from an initial laser pulse. Both radiative and nonradiative recombination of electron-hole pairs takes place over several nanoseconds after the initial excitation pulse. A typical method for collecting time resolved spectra uses a streak camera, which has a temporal resolution of approximately 10 ps (Shah, 1988). In order to obtain better temporal resolution, Mahr and Hirsch developed the upconversion technique (Mahr and Hirsch, 1974). Upconversion is applied in this experiment to obtain sub-picosecond resolution of the luminescence emitted over a 3-ns time period (TRPL). A mode locked Ti:Sapphire laser is used to create extremely short pulses. The beam is split and one leg is used to excite a semiconductor sample. The luminescence from the excited sample is focused inside a nonlinear crystal, where it interacts with a beam that had been split off from the laser source. The wave mixing that occurs within the crystal produces a third beam, with a predictable wavelength, that is collected. The portion of the beam split off to excite the sample will be referred to as the PL beam, and the luminescence signal will be called the PL signal. Together, the PL beam and the PL signal travel an optical path that is equal to the path of the split off laser beam, which will be called the pump beam. The third beam, called the upconverted beam, will only be created when both the PL signal and pump beam are present within the crystal. A pulsed pump beam will therefore act as a light gate and allow for the temporal resolution of the PL signal (Shah, 1988). By varying the optical path of one of the incoming beams, the luminescence from the excited semiconductor can be resolved over time. This process is

depicted in Figure 3.1. This chapter will discuss the theory of upconversion, the methods applied in the experiment to gather the data, and the efficiency of the upconversion process. It will conclude with a description of the sample semiconductors investigated.

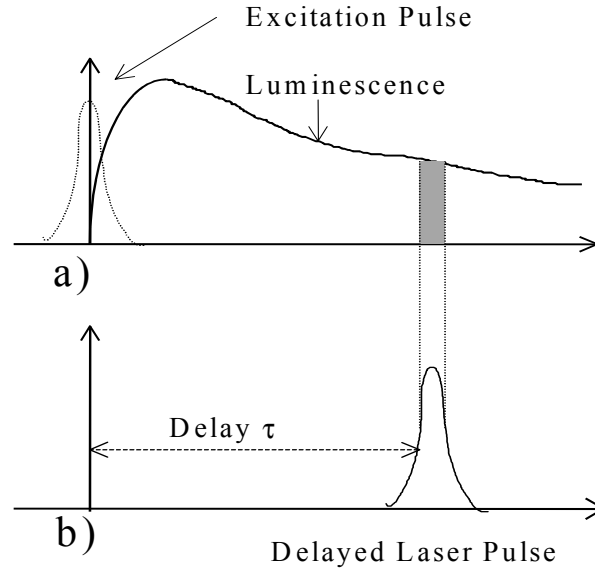


Figure 3.1. Wave mixing resulting in the time resolution of the luminescence. (a) Depicts the luminescence curve over time. (b) Represents the pump beam at some delay time τ .

3.1. Upconversion theory

Upconversion, also called sum frequency generation, is the process of mixing two optical waves to generate a third wave. The interaction required for the upconversion of two optical waves occurs in a non-linear optical medium. A non-linear medium is one in which the polarization density can be expressed as a Taylor series expansion:

$$P_i = \epsilon \chi_{i,j} E_j + 2\epsilon \chi_{i,jk} E_j E_k + \dots, \quad (3.1)$$

where P is the polarization density, E is the induced electric field, ϵ is the permeability of free space, and χ is the susceptibility (Yariv, 1984:504). In this experiment, waves are

mixed in a KTiOAsO_4 (KTA) crystal exhibiting second-order nonlinearity, and higher order terms in the series expansion are considered negligible. If the optical waves are modeled as plane waves, the second order term in Eq (3.1) results in two conditions required for upconversion. The first is the frequency matching condition that dictates:

$$\omega_3 = \omega_1 + \omega_2 \quad (3.2)$$

In this experiment, the pump beam frequency and the peak luminescence frequency from the excited sample sum to the upconverted frequency. Manipulating Eq (3.2) creates an expression based on the conservation of energy used to determine the wavelength of the upconverted photons:

$$\frac{1}{\lambda_{\text{up}}} = \frac{1}{\lambda_{\text{PL}}} + \frac{1}{\lambda_{\text{Pump}}} \quad (3.3)$$

where λ_{up} is the wavelength of the upconverted wave and λ_{PL} , and λ_{Pump} refer to the wavelengths of the PL and pump beams, respectively.

The second condition required for upconversion is the phase matching condition:

$$\vec{k}_{\text{up}} = \vec{k}_{\text{PL}} + \vec{k}_{\text{Pump}} \quad (3.4)$$

where k is the wave vector ($|k| = 2\pi n / \lambda$) illustrated in Figure 3.2. When the law of cosines is applied to Eq (3.4) and k is replaced, the expression becomes:

$$\frac{n_{\text{up}}^2}{\lambda_{\text{up}}} = \frac{n_{\text{PL}}^2}{\lambda_{\text{PL}}} + \frac{n_{\text{Pump}}^2}{\lambda_{\text{Pump}}} - 2 \cdot \frac{n_{\text{up}} \cdot n_{\text{PL}}}{\lambda_{\text{up}} \cdot \lambda_{\text{PL}}} \cdot \cos(\pi - \gamma) \quad (3.5)$$

where γ is the angle between the PL and pump wave vectors and n_{up} , n_{PL} , and n_{Pump} are the refraction indices seen by the upconverted beam, the PL signal, and the pump beam.

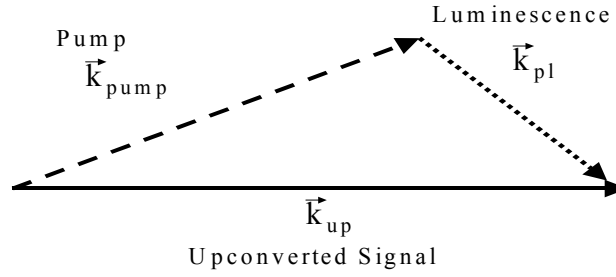


Figure 3.2. Phase matching geometry required for upconversion. The pump beam and PL beam enter the crystal at 20°

Fenimore (1995) gives the Sellmeier equations, which express index of refraction as a function of wavelength for the KTA crystal in terms of the three principal axes n_x , n_y , and n_z . The crystal used here is cut at an angle $\Phi = 43^\circ$, where Φ is the angle between the crystal axis and the normal to the surface in the X-Z plane. The refraction indices in the ordinary and extraordinary polarizations can now be written in terms of the crystal axis indices:

$$n_o(\lambda) = n_y(\lambda)$$

$$n_e(\lambda) = \frac{n_x(\lambda) \cdot n_y(\lambda)}{\sqrt{n_z(\lambda)^2 \cdot \cos(\theta)^2 + n_x(\lambda)^2 \cdot \sin(\theta)^2}}, \quad (3.6)$$

where θ is the angle between the extraordinary beam and the z axis. When the laser beam is split, the PL beam is orientated to be ordinary and the pump beam is extraordinary.

The properties of the KTA crystal dictate that the upconverted wave will then be ordinary. With all other parameters known, Eq (3.6) can be solved for θ for any given wavelength. Recall that θ is the angle of the pump beam to the z-axis and can be changed by simply rotating the crystal. A MathCad program (See Appendix A.1) incorporates

these equations so that it will provide the crystal tilt required to meet the phase matching condition for a given experimental set up. The next section will describe how the experiment was constructed to mix these waves inside a crystal and collect the resulting upconverted beam.

3.2. Experimental Set Up

Capt William Cooley first developed the upconversion experiment at AFIT in 1997. A schematic of the experimental set up can be seen in Figure 3.3. This section details the laser source used for excitation, the optical path, and the collection of the photoluminescence and upconverted signal.

3.2.1. Laser Source

A Coherent Mira 900 mode-locked Ti:Sapphire laser operating at 1.5 watts average power produced the pulses required for upconversion. The laser's repetition rate is 76 MHz with a center wavelength of 809 nm. The mode-locked pulses excite the sample every 13.2 ns, allowing time to study the luminescence decay. The pulse width, which establishes the temporal resolution of the luminescence decay, is 122 fs. The Ti:Sapphire is optically pumped by a 12.0 watt Spectra Physics argon-ion (Ar^+) laser. The spectral and temporal aspects of the Ti:Sapphire beam can be seen in Figure 3.4.

The pulse width was measured using an INRAD Model 5-14BX Autocorrelator and verified using the upconversion experiment. The autocorrelator could produce highly accurate results much faster than the upconversion experiment. The autocorrelator splits the laser into two paths and focuses the beams together inside a non-linear crystal.

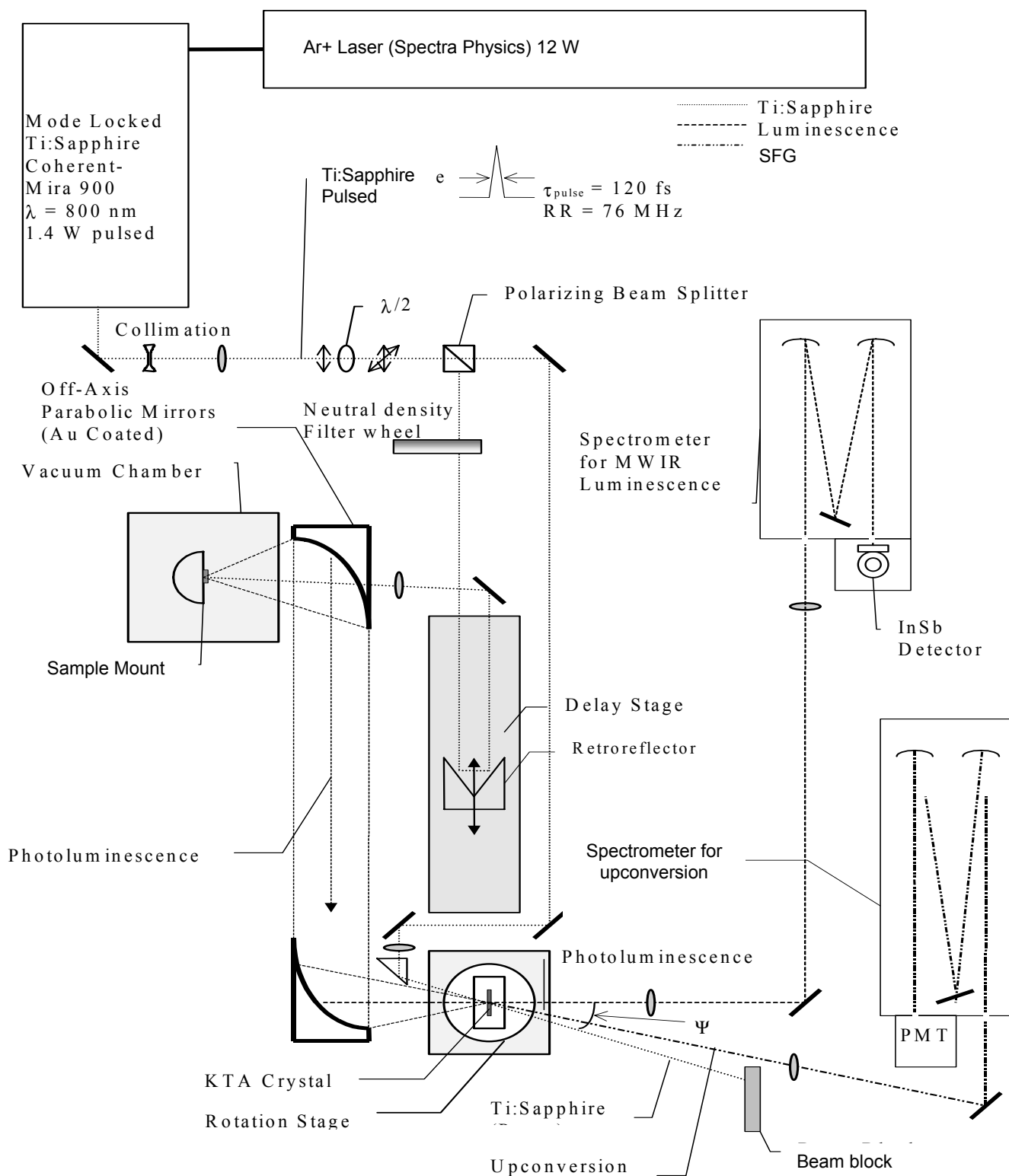


Figure 3.3. Experimental set up in TRPL experiment. The Ti:Sapphire laser creates a 122 fs pulse that is split into two paths. The PL beam travels through a delay stage before exciting the sample. Luminescence is collected and mixed with the pump beam in the KTA crystal. The upconverted beam is then directed to the spectrometer and photon counter.

A LiIO_3 crystal is used to create an upconverted beam. One path passes through a delay stage that varies the optical path length, while a detector collects the upconverted beam. The result, which can be seen in Figure 3.4, is a temporal pulse with a measurable width.

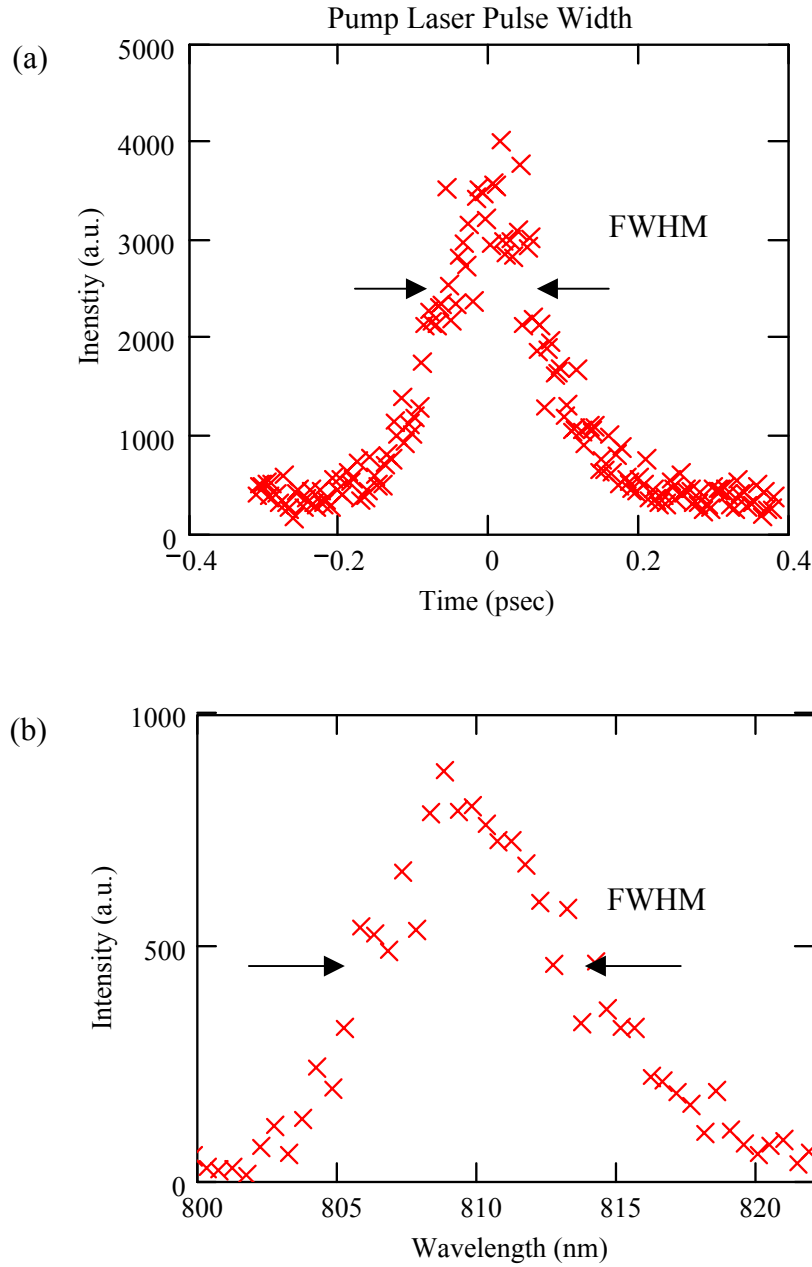


Figure 3.4. (a) Temporal pulse width of Ti:Sapphire laser. FWHM is measured to be $\Delta t_m = 188$ fs. A correction factor of 0.648 is used to obtain an actual pulse width of $\Delta t_a = 122$ fs (b) Spectral width of Ti:Sapphire pulse with a FWHM of 10 nm.

The manufacture suggests using a sech^2 function to fit the line shape, which gives rise to a conversion factor of 0.648 to convert from the measured pulse width to the actual pulse width.

Knowledge of the focused laser spot size, both within the crystal and on the sample, is critical for performing the upconversion experiment and is used extensively in the data analysis seen in Chapter 4. A Coherent-Mode Master was used to measure the beam diameter as well as the M^2 value of the beam. The M^2 value is a relative term comparing the beam profile to that of a Gaussian profile. The Ti:Sapphire laser produced a beam with an M^2 value of 1.3, which means the beam waist will be 1.3 times the size of a diffraction limited Gaussian beam waist. The beam diameter was measured in two places in the beam path to be $6.85 \pm .032$ mm. The lens used to focus the pump beam and PL beam on the crystal have a focal length of 200 mm and 300 mm, respectively. Assuming the beam is Gaussian, the spot sizes on the crystal can be calculated by:

$$2 \cdot \omega = \frac{4}{\pi} \cdot \frac{\lambda \cdot f}{D}, \quad (3.7)$$

where 2ω is the focused beam diameter, f is the focal length, and D is the beam diameter just before reaching the lens. Using this method, the pump beam spot size was determined to be 39.1 ± 0.15 μm and the PL spot size was 58.5 ± 0.20 μm . The M^2 value of the beam was incorporated in the spot size calculations to account for the beam's shape. An analysis of the accuracy required of the spot size measurement is included in Chapter 4. When operating properly, the Ti:Sapphire laser produced a very stable beam with consistent pulse, which proved crucial in day-to-day data collection.

3.2.2. Optical Path

Once the beam leaves the Ti:Sapphire laser, wavelengths below 700 nm are filtered out, and the beam is expanded and collimated before it reaches a beam splitter, as seen in Figure 3.3. A $\lambda/2$ wave plate is used to vary the polarization of the beam. The beam splitter separates the beam into horizontal and vertical components. By adjusting the $\lambda/2$ wave plate, the power ratio in each leg can be varied. The PL beam is the portion that will excite the sample creating a PL signal. The pump beam will propagate a fixed distance comparable to the combined distance the PL beam and PL signal will travel. The PL signal and pump beam will be focused onto the nonlinear crystal causing them to mix and produce an upconverted beam.

3.2.2.1. PL Path

The PL path is comprised of the PL beam and the PL signal. The PL beam begins when the vertically polarized beam exits the beam splitter, passes through a neutral density filter, and encounters a delay stage seen in Figure 3.3. The delay stage consists of a gold-coated retroreflector on a sliding mount that allows the optical path length of this leg to be varied. The ability to change the optical path of one beam with respect to the other allows the luminescence decay to be mapped, as described by Figure 3.1. The beam makes two passes through the 30-cm-long delay stage, which allows the path length of the PL beam to vary by 4 ns ($4 \times 30 \text{ cm} / c = 4 \text{ ns}$). The PL beam is then focused onto the sample being investigated, which is mounted in a vacuum chamber. A gold-coated, 90° off-axis parabolic mirror with a focal length of 150 mm directs the luminescence, or PL signal, from the sample to an identical mirror, which focuses the luminescence on the

nonlinear crystal mounted on the rotation stage. The two mirrors form a one-to-one imaging system, with the sample in the object plane and the crystal in the image plane.

3.2.2.2. Pump Beam Path

The pump beam is horizontally polarized when it exits the beam splitter and travels over an optical path similar in length to the PL path. A 200-mm lens is used to focus the beam down to a spot within the nonlinear crystal, as seen in Figure 3.3. A prism is used to create a 20° angle between the pump beam and the PL beam. The relative angle between the beams is fixed and used in Eq (3.5) when determining the crystal tilt angle required for upconversion. The pump beam is mixed with the PL signal to create the upconverted beam.

3.2.2.3. Beam Overlap

The upconversion process relies on two optical waves interacting with one another to generate a third wave (Saleh and Teich, 1991:748). This requires that the waves overlap in space and time in order to create an upconverted beam. Spatial overlap was achieved by replacing the non-linear crystal with a pinhole in a similar mount on the rotation stage seen in Figure 3.3. Both the pump beam and the PL signal were focused through a 100- μm pinhole initially to determine coarse alignment. Although the beam spot sizes were calculated to be 39.1 and 58.5 μm for the pump beam and PL signal, the 100- μm pinhole did not ensure sufficient overlap for upconversion. A 25- μm pinhole was then used to make fine adjustments and ensure maximum spatial overlap of the two beams.

Temporal overlap was achieved by mixing the pump beam with itself to create an upconverted beam. The sample was moved out of the PL beam path, and the laser's specular reflection off of the cold finger in the sample chamber was collected rather than the luminescence. This process is identical to the method used by the autocorrelator discussed earlier, and a LiIO_3 crystal is used to mix the two beams. The resulting upconverted signal is in the visible spectrum, so that it is easily seen when the optical path lengths of the two legs are equal. The delay stage was moved incrementally until the upconverted beam was observed. This procedure confirmed that both beams were present in the same space at the same time in the crystal.

3.2.4. Signal Collection

This experiment requires that standard luminescence data be collected on each sample to identify the spectral characteristics of the sample's emission prior to performing upconversion. The design of the experiment allows for luminescence data to be taken with minimal impact to the upconversion configuration.

3.2.4.1. Photoluminescence experiment

No wave mixing is required when taking time-averaged photoluminescence data. The nonlinear crystal is removed from the rotation stage in Figure 3.3 and the pump beam is blocked. The PL beam excites the sample and parabolic mirrors direct the luminescence. The PL signal is then collected and re-collimated by a CaF_2 lens that will pass light in the IR spectrum. A second CaF_2 lens focuses the signal on the entrance slit of a $\frac{1}{2}$ meter SPEX spectrometer with a 4- μm -blaze grating. The grating has 1200

grooves/mm with a calculated resolution of 5 nm. A Standard Research Lock-in Amplifier amplifies the signal from a single element InSb detector.

3.2.4.2. TRPL experiment

The nonlinear crystal used to mix the PL and pump beams in this experiment is a 1-mm-thick KTA crystal cut so the z-axis is 43° from the incident normal. The pump and PL beams must overlap in time and space within the crystal for them to mix and create the upconverted beam. With all other parameters fixed, the wavelength of the luminescence signal, typically 3.1- 4.5 μm , dictates the crystal tilt angle and the exit angle of the upconverted beam. A collection lens is used to focus the upconverted signal onto the entrance slit of a $\frac{3}{4}$ meter SPEX spectrometer. The grating used has 1200 grooves/mm with a calculated resolution of 3.3 nm. The signal is collected by a GaAs photomultiplier tube cooled to 0° C and biased at 2000 V. The signal is amplified and sent to a Standard Research SR400 photon counter, which passes data to a computer interface used to control the experiment. The computer allows for either the spectrometer or the delay stage to be incremented while taking photon counts.

In order to record the luminescence temporal evolution, the spectrometer was tuned to the peak upconverted wavelength, and the crystal angle was set to maximize the upconverted signal. The delay stage was then moved incrementally as intensity data was recorded. The photon counter integrated the counts it received over 30 seconds at each increment in the delay. When investigating the decay of the luminescence, the experiment was set to record data every 50 ps over a 3 ns time period. The number of data points allowed for a high confidence curve fit to analyze the luminescence decay.

More data points were required to investigate the luminescence rise, which occurs over the first 25-30 ps. Data was recorded every 2 ps over a 50 ps time period to examine the rise time.

Spectral data was taken by setting the delay stage at one position and scanning over the spectra of the upconverted signal. The spectrometer scan speed was dictated by the resolution of the grating calculated to be 3.3 nm. In order to match the grating resolution, a speed of 10 nm/min was chosen so that each data point would represent the intensity over 5 nm. This procedure was repeated for several fixed times over the 3-ns period after the excitation pulse.

Another method to obtain spectral data was also attempted that has been used in previous experiments (Franz, 1997:33). The upconversion experiment was run to measure the time decay of the luminescence at a fixed wavelength. The wavelength was then incremented and another time decay plot was taken. All of the points corresponding to a specific delay time were then put together to create a spectral plot at a snapshot in time. This method produces significantly more data points in time, but many measurements would have to be taken to obtain a sufficient number of spectral points. The analysis of this data focuses on the spectral data, which is improved with more data points. In addition, the phase matching condition to upconvert specific wavelengths required a crystal tilt angle unavailable in this experimental set up. If the crystal is tilted between 18.8° and 20.5° , the specular reflection retraces the path of the pump beam and interferes with the mode-locking of the Ti:Sapphire.

3.3. Upconversion Efficiency

When the upconversion experiment is used to measure the time decay luminescence, the crystal is turned to the phasematching angle in order to satisfy Eq (3.4), which will maximize upconversion. As the crystal is tilted away from the phasematching angle so that Eq (3.4) is no longer true, the upconversion efficiency decreases rapidly until upconversion is no longer possible. Spectral data was taken in this experiment by fixing the crystal to the optimal phasematching angle to upconvert the peak PL signal. In order to ensure that the spectral tails of the luminescence can be upconverted, the acceptance angle of the crystal must be calculated. The acceptance angle is the solid angle, which is centered about the phasematching angle, over which upconversion can still take place. The acceptance angle is given by:

$$\Delta\phi = \frac{2.78 \cdot n \cdot \lambda_{pl}}{L \cdot \left(1 - \frac{n \cdot \lambda_{SFG}}{\theta \cdot n \cdot \lambda_{pl}} \right)}, \quad (3.8)$$

where L is the crystal thickness (Shah, 1988). The index of refraction for the PL signal ($n = 1.74$) and the upconverted signal ($n_{up}=1.85$) are calculated using the program in Appendix A.1. The sample with the broadest spectra, spanning from 3.1 to 3.7 μm , was chosen to analyze the acceptance angle. The calculated acceptance angle for Sample 91 is $\Delta\phi = 0.021$ steradians. This solid angle is converted to a planar angle using the following equation:

$$\phi = 2 \cdot \pi \left(1 - \cos \left(\theta_{max} \right) \right) . \quad (3.9)$$

The resulting planar angle that will be accepted by the crystal for upconversion is $\pm 4.6^\circ$. The phasematching angles for the Sample 91 PL spectra are $19.1^\circ \pm 3.5^\circ$, which is within the acceptance angle for all wavelengths in the spectra. While the entire spectra can be upconverted, the efficiency of the upconversion process will decrease as the crystal tilt angle moves away from the phasematching angle.

Cooley calculated the upconversion efficiency for this experiment to be approximately 0.1% for perfect phasematching of the incoming beams (Cooley, 1997:81). This peak efficiency is based on the crystal parameters, the wavelengths being mixed, and the ratio of beam power to area on the crystal, and should remain constant for a specific experimental set up. When the phasematching condition is no longer met, Eq (3.4) becomes:

$$\vec{\Delta k} = \vec{k}_{PL} + \vec{k}_{Pump} - \vec{k}_{up} \quad (3.10)$$

The upconversion efficiency will fall off as (Shah, 1988):

$$\frac{\eta(\Delta k)}{\eta_{peak}} = \frac{\sin(L_e \cdot \Delta k)^2}{(L_e \cdot \Delta k)^2}, \quad (3.11)$$

where L_e is the effective length of the crystal, which may be shorter than the actual length of the crystal.

Dmitriev's method for determining the effective length for an upconversion experiment with short laser pulses is to compare the crystal length to the quasi-static length given by:

$$L_{qsp} = (v \cdot \Delta \omega)^{-1}, \quad (3.12)$$

where $\Delta\omega$ is the spectral pulse width and v is the inverse group velocity mismatch given by:

$$v = u_1^{-1} - u_2^{-1}, \quad (3.13)$$

where u_1 and u_2 are the group velocities for the two waves being mixed in the crystal (Dmitriev *et al.*, 1997:60). The calculated quasi-static length was 112 μm , which is significantly shorter than the actual crystal length of 1 mm. Cooley calculated the effective length for this experiment to be $L_e = 106 \mu\text{m}$, taking into account all spatial and temporal considerations (Cooley, 1997:82-84). The effective length used will be the quasi-static length ($L_e = 112 \mu\text{m}$) because the simplified approach proposed by Dmitriev produces results agreeable with Cooley.

The effective length can now be used in Eq (3.11) to determine the upconversion efficiency for a particular experiment. The sample with the widest spectral width was used to calculate Δk values for various wavelengths within the PL spectra. The relationship between the upconversion efficiency fall off and wavelength for a particular semiconductor can be seen in Figure 3.5. The upconversion efficiency is greater than 97% at the FWHM of the spectrum and greater than 90% across the entire spectrum. The variation in efficiency will introduce error in spectral luminescence data, but is small enough to allow for qualitative comparisons of carrier temperature derived from this data.

3.4. Sample Description

The four samples investigated in this experiment were laser structures provide by Lincoln Laboratory at the Massachusetts Institute of Technology (MIT). Specific information on growth procedures has been published (Turner, 1995). Cooley (1997) and

McKay (2000) have each investigated some of the samples tested in this experiment. The rationale behind examining these semiconductors is to provide a uniform comparison of different type structures using a consistent method. In addition, data involving coefficient reliability, luminescence rise time, and spectral decay was collected in order to better understand the carrier dynamics in each sample.

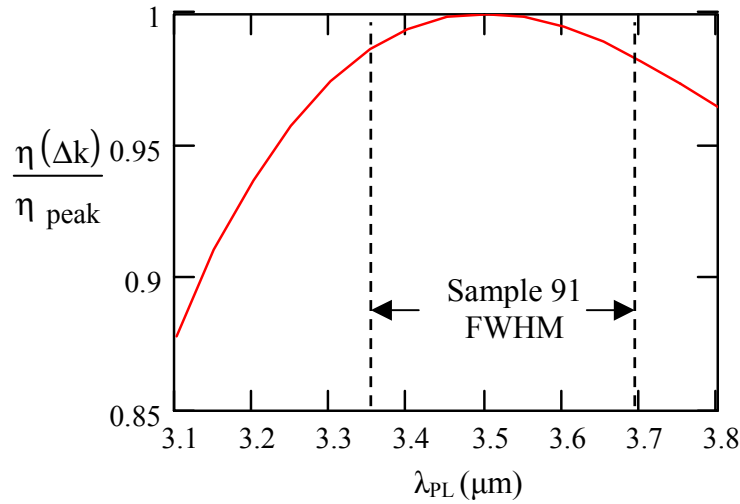


Figure 3.5. Upconversion efficiency compared to peak efficiency over the luminescence spectra of Sample 91. The Sample 91 PL curve peaks at 3.5 μm s with a FWHM indicated by the dashed lines in the figure.

Sample “B” is a multiple quantum well type I structure grown by molecular beam epitaxy (MBE). The confinement of electrons and holes occurs in the same material in a type I structure. The well structure is made up of $\text{InAs}_{0.935}\text{Sb}_{0.065}/\text{In}_{0.85}\text{Al}_{0.15}\text{As}_{0.9}\text{Sb}_{0.1}$ and can be seen in Figure 3.6.

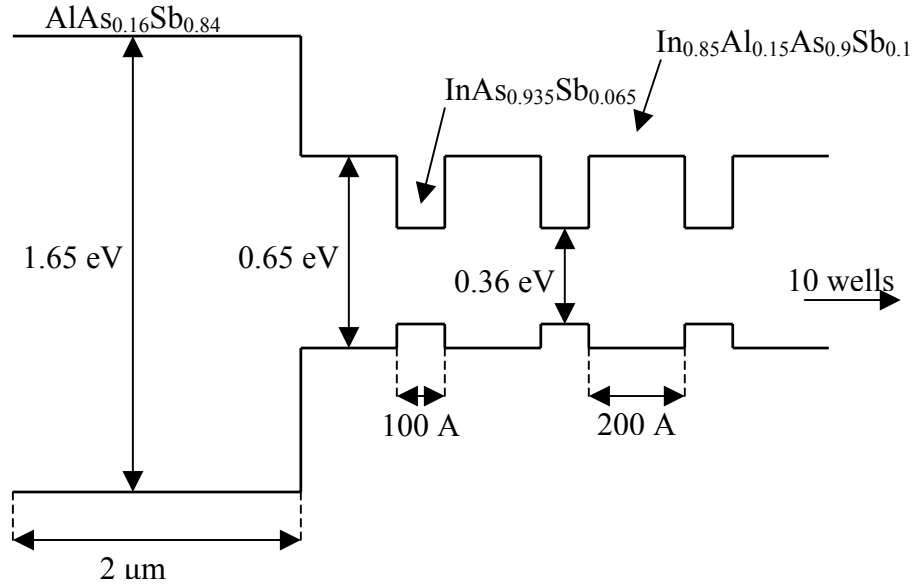


Figure 3.6. Sample B quantum well structure. Energy diagram with offset bands and excitation energy drawn to scale. Well and Barrier widths are also included.

Samples 88, 90, and 91 are $\text{InAs}/\text{Ga}_{0.85}\text{In}_{0.15}\text{Sb}$ type II quantum well structures also provided by MIT. A Type II structure allows for electron confinement in one material, while holes are confined in the neighboring material. The different samples are identical to each other except for varying well widths, which can be seen in Figure 3.7. Time integrated photoluminescence was taken on each of the samples and can be seen in Figure 3.8. The data was taken with the sample held at 77 K and an excitation power of 600 mW . Sample B and sample 91 were the brightest samples. As the width of the wells in the type II structure becomes wider, the peak wavelength shifts to lower energies. This result is predicted by Eq (2.1), which states that energy levels in a quantum well are inversely proportional to well width.

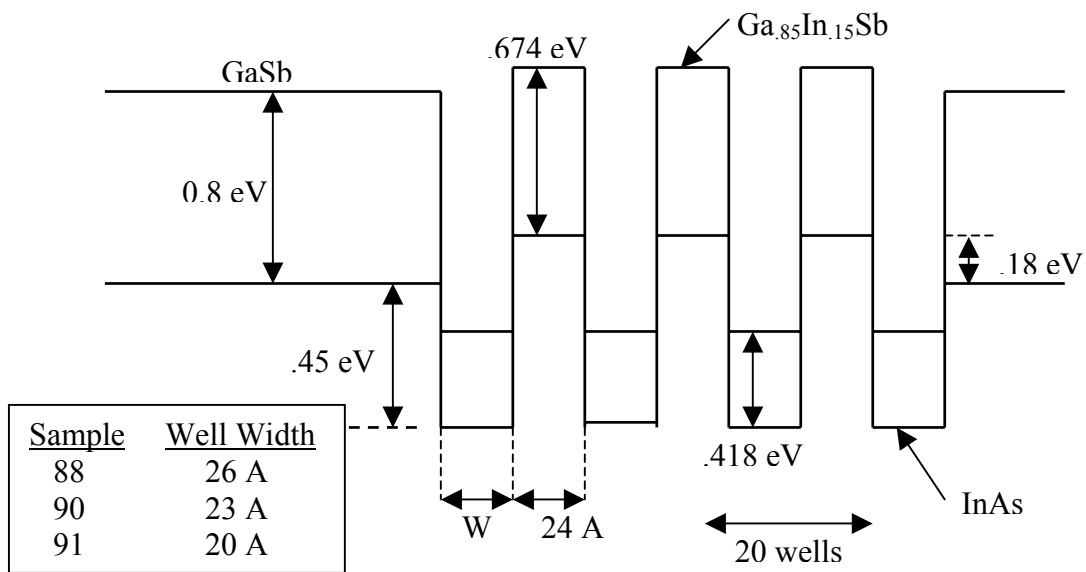


Figure 3.7. Sample 88, 90, and 91 quantum well structure. Energy diagram with offset bands and excitation energy drawn to scale. Well and Barrier widths are also included.

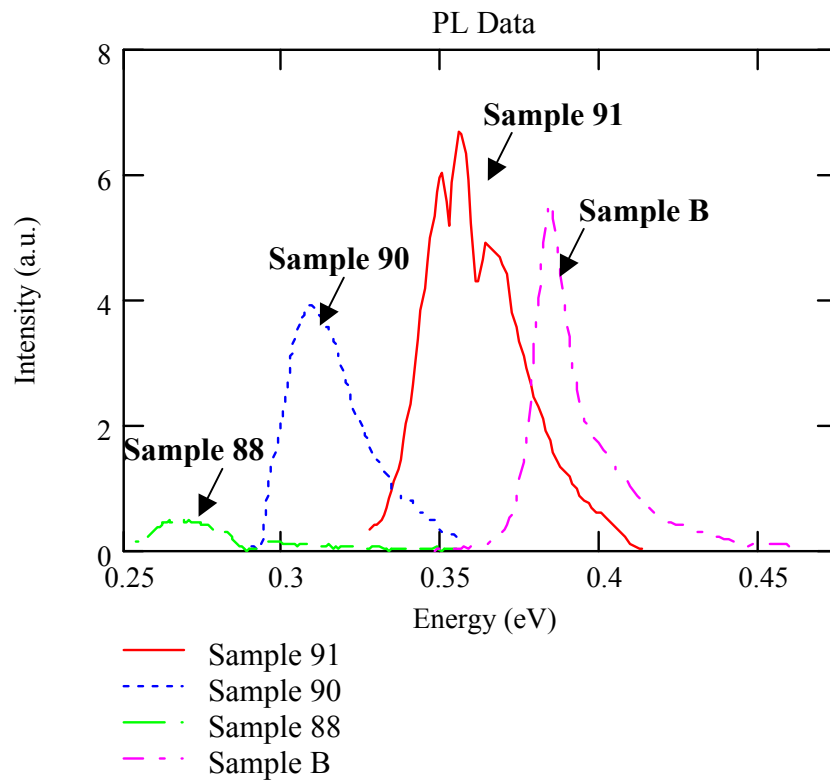


Figure 3.8. Photoluminescence curves for each sample tested. Sample B is a type I structure Sample 88, 90, and 91 are type II. Intensities are shown as true scale.

4. Data Analysis and Results

The data collected in the upconversion experiment described in the previous chapter provides both time resolved luminescence and spectral luminescence intensities radiated by the tested samples. Time resolved plots are used to determine the recombination coefficients and allow for a qualitative comparison of carrier relaxation into the quantum well structure. Spectral data is used to extract carrier temperature information. Recombination rates, carrier relaxation, and carrier temperature are all critical factors that influence laser performance. This chapter will discuss the time resolved and spectral results, and the analysis performed on the experimental data will be used to draw conclusions on the device performance.

4.1. Determining Recombination Coefficients

The time resolved luminescence decay curves recorded over 3-ns are used to determine the recombination coefficients for the samples. As mentioned earlier, the Auger coefficient is of greatest importance because it is detrimental to device performance and can be reduced by altering the design of the structure (Lindle, 1995). There have been some discrepancies in calculating recombination rates from luminescence data in previous reporting, with Auger rates ranging from 10^{-26} cm⁶/s (Lindle, 1995) to 10^{-31} cm⁶/s (Cooley, 1997) for mid-IR semiconductor type I structures and from 10^{-28} cm⁶/s (Meyer, 1998) to 10^{-32} cm⁶/s (McKay, 2000) in type II structures. The factors that lead to the greatest uncertainty in calculating recombination coefficients when conducting time resolved luminescence experiments arise when determining carrier densities and curve fitting the data. Approximations to unknown material parameters

have a significant impact on calculating carrier densities, and result in recombination coefficients from different experiments that cannot be compared. The theory remains sound and allows for different materials to be compared provided the calculations are subject to identical assumptions and error is minimized. This section deals with the analysis performed to determine recombination coefficients and the error associated with assumptions that have been made.

4.1.1. Analysis of Decay Curve

The equation that describes the change in carrier density due to spontaneous emission in a semiconductor is:

$$-\frac{dn}{dt} = A_{SRH} \cdot n + B_{rad} \cdot n^2 + C_{Auger} \cdot n^3, \quad (4.1)$$

where n is the carrier density, and A_{SRH} , B_{rad} , and C_{Auger} are coefficients associated with the recombination processes discussed in Chapter 2. Eq (4.1) can be solved for carrier density as a function of time if the initial condition, or the carrier density at time $t = 0$, is known.

The data collected in the upconversion experiment yields luminous intensity at various times, as depicted in Figure 4.1.

A relationship between carrier density and luminescence allows the collected data to be transformed to carrier densities at the same time intervals. Eq (4.1) can then be fit to the data, and the coefficients extracted. These coefficients are parameters of the material and allow for comparison between different quantum well types and sizes. The carrier densities must be known before a relationship between carrier density and luminescence can be determined. The method employed, which is taken from Sermage

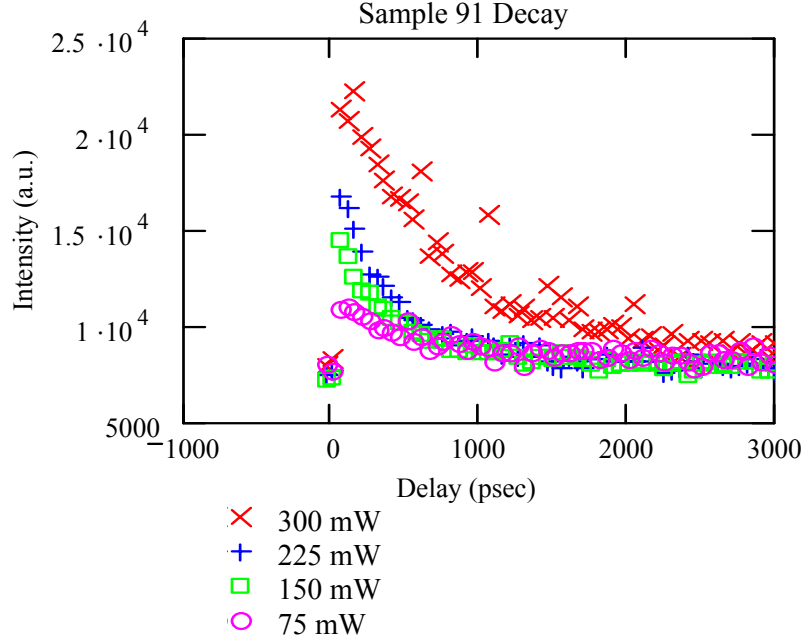


Figure 4.1. Sample TRPL data collected. The intensity of the upconverted signal from an optically excited quantum well structure is plotted over 3 nanoseconds. Multiple curves indicate varying excitation power.

(Sermage, 1997) and adapted by Cooley, allows the maximum carrier density created in the structure to be written as a function of laser input power, beam sizes, and material parameters:

$$n(t_0) = \frac{E}{h \cdot \nu} \cdot \left(\frac{2}{N_{qw} \cdot \pi \cdot w_{pl}^2 \cdot t_B} \right) \cdot (1 - R_s) \cdot 1 - e^{-\alpha \cdot N_{qw} \cdot (t_B + t_{bar})} \cdot \frac{1}{1 + \frac{w_p^2}{w_{pl}^2}} \quad (4.2)$$

The initial term represents the number of photons per pulse. E is the energy per pulse and is determined by taking the average power divided by the repetition rate of the laser. The second term represents the number of carriers per unit volume. N_{qw} is the number of quantum wells in the sample, t_B is the thickness of the quantum well, and w_{pl} and w_p are the waist sizes of the PL beam and pump beam defined by the $1/e^2$ intensity

points. The third term indicates the power loss associated with reflection off the sample.

R is the reflectance and can be measured directly or calculated by:

$$R_s = \left(\frac{n_s - 1}{n_s + 1} \right)^2, \quad (4.3)$$

where n_s is the index of refraction of the semiconductor. The fourth term represents the amount of energy absorbed by each quantum well. The term α represents the absorption coefficient and t_{bar} is the barrier layer thickness. The final term is a beam overlap efficiency required because the PL and pump beam are not focused to the same size, resulting in a loss of photons available for upconversion. This equation was modified for type II structures (McKay, 2000) to account for the offset wells:

$$n(t_0) = \frac{E}{h \cdot \nu} \cdot \left(\frac{t_{\text{InAs}} + t_{\text{GaInSb}}}{N_{\text{qw}} \cdot \pi \cdot w_{\text{pl}}^2 \cdot t_{\text{InAs}} \cdot t_{\text{GaInSb}}} \right) \cdot (1 - R_s) \cdot 1 - e^{-\alpha \cdot N_{\text{qw}} \cdot (t_{\text{InAs}} + t_{\text{GaInSb}})} \cdot \frac{1}{1 + \frac{w_{\text{p}}^2}{w_{\text{pl}}^2}}, \quad (4.4)$$

where t_{InAs} and t_{GaInSb} are the thickness' of corresponding layers in the material.

The initial carrier density equation is a large contributor to the discrepancies in reporting recombination coefficients on specific materials. The initial carrier density equations described in Eq (4.2) and Eq (4.4) make some key assumptions. As Cooley pointed out, the carrier loss that occurs during the pulse is considered negligible, and hence ignored (Cooley, 1997:117). The closest index of refraction for the substrate GaSb is determined experimentally and is an approximation to the index of the QW structure (Madelung, 1991). The beam overlap was calculated assuming a Gaussian beam profile.

Finally, the absorption coefficient is determined by ellipsometry for Sample B, and unavailable for Sample 88, 90, and 91. The uncertainties in these values lead to uncertainties in the conversion of luminescence to carrier densities, and therefore, the recombination coefficients.

The error in estimating the carrier density is investigated by determining the impact each parameter in Eq (4.2) has on the computed initial carrier density. There are uncertainties in the absorption coefficient, index of refraction, and beam waist size that have been decreased through experimentation and a review of the literature. A range of absorption coefficients was used to determine carrier densities, and the percent change in carrier density over that range was calculated. This process was repeated for each unknown parameter, and the results can be seen in Table 4.1. This analysis indicated that the uncertainty in the absorption coefficient has the strongest influence on the carrier density.

While the absorption coefficient was determined experimentally for Sample B, no information is available for type II structures. An absorption coefficient of $2 \times 10^6 \text{ cm}^{-1}$ was determined by ellipsometry on Sample B (Cooley, 1997:120). This value was used in the analysis for all four samples. It is expected that the absorption coefficient for type II structures is within an order of magnitude of Sample B.

Cooley measured the effective index of refraction of Sample B by ellipsometry to be $n = 3.87$ (Cooley, 1997:120). The closest approximation to the index for the type II structures is based on the index of the GaSb substrate, which is $n = 4.39$ (Madelung, 1991:120). The index is required to determine the reflectivity of the semiconductor, so the amount of power reflected can be accounted for. Without considering quantum

effects, 39% of the light traveling from air to GaSb will be reflected assuming normal incidence. The next material in the quantum well is AlAsSb, with a lower index of approximately $n = 3.2$. Only 0.1% of the remaining light will be reflected, which is negligible. This analysis, however, does not take into consideration the fact that the semiconductor layers are all significantly less than one wavelength of the incoming laser. Therefore, experimental measurements of the reflectance were conducted in order to reduce the uncertainty introduced in Eq (4.2) by the index of refraction. The beam power was measured before and after reflection off each sample. The reflectance is then the ratio of reflected to incident power. This calculation assumes a perfectly specular reflection at the face of the sample. Eq (4.3) was used to determine effective indices of $n = 4.5$ for Sample B and 4.3 for the type II structures based on the experimental reflectance values.

Finally, the beam spot sizes were calculated using experimental measurements and Eq (3.7) with an error of less than $0.2 \mu\text{m}$. The range of spot sizes used in this analysis accounts for the uncertainty in the calculated spot size.

Table 4.1. Analysis of error in unknown parameters used to calculate the carrier density. (1) determined experimentally by ellipsometry from Cooley. (2) determined experimentally by Mode Master using scanning knife edge method.			
Variable	Value used	Range	% change in carrier density over range
α	$2 \times 10^6 \text{ cm}^{-1}$ (1)	$7 \times 10^5 \dots 7 \times 10^6$	288
n	4.5 (type I) 4.3 (type II)	4.3...4.5	1.8
$2 w_p$	$39 \mu\text{m}$ (2)	$\pm 0.15 \mu\text{m}$	0.5
$2 w_{pl}$	$58.5 \mu\text{m}$ (2)	$\pm 0.20 \mu\text{m}$	< 0.1

Once the initial carrier densities are known for various pump powers, a curve can be fit to the data to develop a relationship for carrier density as a function of luminescence. The initial carrier density is computed for a number of excitation powers. These carrier densities were plotted against the experimentally determined luminescence intensities at the same excitation powers. The following fitting function was used to approximate the data:

$$n(L) = u_0 \cdot L + u_1 \cdot L^{u_3} \quad (4.5)$$

The resulting fit has a R^2 value of 0.98 and is shown in Figure 4.2. This fit is then used to calculate all of the carrier densities ($t > 0$) from the luminescence data collected.

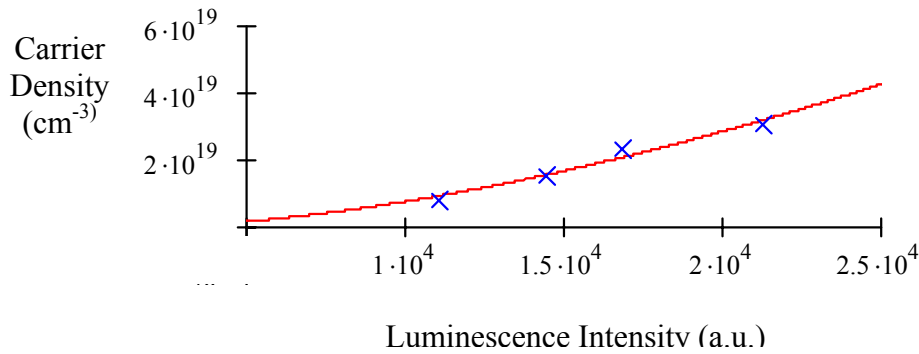


Figure 4.2. Carrier density as a function of luminescence intensity. Data points are the initial ($t = 0$) carrier densities generated by the laser pulse, which were calculated using Eq(4.4). The solid line represents a fitting function found in Eq (4.5) used to related carrier densities at $t > 0$ to luminescence intensities.

Curve fitting the carrier density rate equation, Eq (4.1), to the data collected has proven difficult (McKay, 2001). Simultaneously fitting four parameters that are 10^{41} apart in magnitude is not an easy task, and the ambiguity in reported recombination

coefficients has been noted (Jang and Flatte, 1998). Previous researchers have used different methods to reduce the number of fitting parameters to solve this problem. The work done at the University of Iowa, cited in the above paper, uses a calculated radiative coefficient and attempts to isolate the A_{SRH} coefficient. McKay attempted to fit all three coefficients simultaneously and relied on the calculated initial carrier density. This paper will use a combination of these methods to find the parameters that yield the best fit to the data.

SRH recombination is assumed to dominate carrier recombination in the low carrier regime. Figure 4.1 shows carrier densities beginning at $t = 0$ when the excitation pulse arrives. These points actually represent the luminescence decay 13.2 ns *after* the previous excitation pulse. The SRH coefficient can be estimated independently by considering the carrier densities in the region of 2.5 ns to 13 ns. If all other terms in the recombination rate equation Eq (4.1) are ignored, then carrier densities in this region can be described by a simple exponential decay. A fit to the data will allow A_{SRH} to be determined independently, reducing one of the parameters in Eq (4.1). The curve fit to determine A_{SRH} for Sample 91 at 300 mW excitation power with a $R^2 = 0.99$ is shown in Figure 4.3. The fit yields an $A_{\text{SRH}} = 3.4 \times 10^7 \text{ s}^{-1}$. SRH is commonly reported as a lifetime measured in nanoseconds with a value of A_{SRH}^{-1} . The SRH lifetime for this fit is 29.4 ns.

The initial carrier density is another key parameter required to solve the differential equation Eq (4.2). Although the initial carrier density was calculated theoretically, there is error in this term as was discussed earlier. If the calculated initial carrier density is used as the initial condition in solving Eq (4.1), unwarranted

weight has been placed on this data point, which forces the fitting curve to go through this point. The initial carrier density found from Eq (4.2) is used as an estimate in the iteration process used to fit all four parameters.

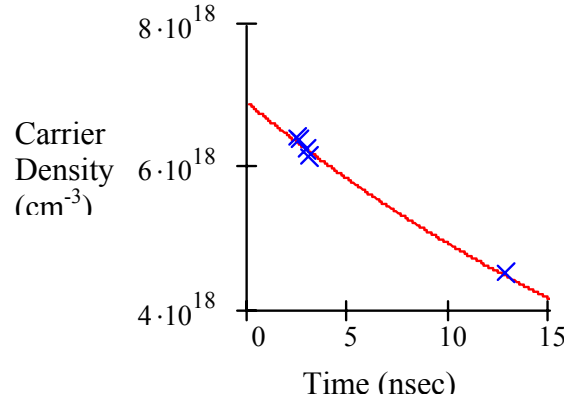


Figure 4.3. Curve fit to estimate A_{SRH} . SRH recombination is assumed to dominate after 2.5 ns. A_{SRH} is determined by fitting an exponential decay curve to the data.

Initial estimates for A_{SRH} and the initial carrier density are used in the recombination rate equation Eq (4.1). A range of B_{rad} and C_{Auger} coefficients are used, and the resulting fit is compared to the data set by the following equation:

$$\text{Error} = \sum_i \left(n(t_i) - Y_i \right)^2, \quad (4.6)$$

where $n(t)$ is the predicted carrier density based on the solution to Eq (4.1), and Y is the data point taken at the same time. A surface plot of the squared error resulting from any combination of B_{rad} and C_{Auger} coefficients can be made, as shown in Figure 4.4.

The minimum on this surface represents the best fit for a given A_{SRH} and initial carrier density. A number of these surfaces were plotted for a series of A_{SRH} and initial carrier

densities. While this is a brute force method of approaching the problem, it will result in the set of coefficients that yield the smallest error. A_{SRH} and the initial carrier density were then varied, and the minimum error point on the B_{rad} and C_{Auger} surface was recorded. The result is another surface plot, shown in Figure 4.5, with a minimum point that represents the unique set of coefficients that best fits the experimental data. This plot was made based on data taken from Sample 91 at 300 mW. Each point on the surface represents the minimum error obtained from a surface plot like the one in Figure 4.4.

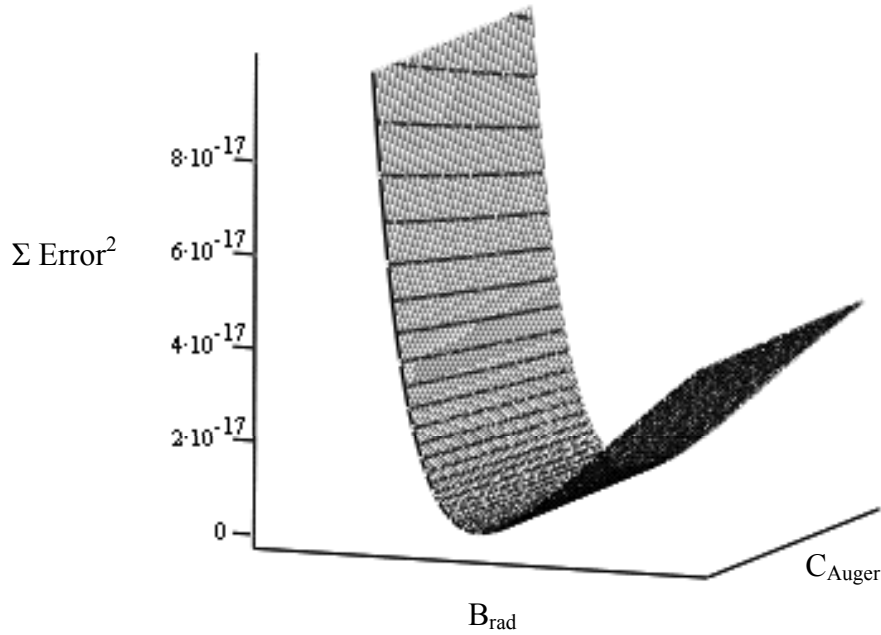


Figure 4.4. Error surface resulting from the fit of Eq (4.1) to the experimental data as a function of B_{rad} and C_{Auger} . The minimum point on this surface represents the best fit for a given A_{SRH} and initial carrier density.

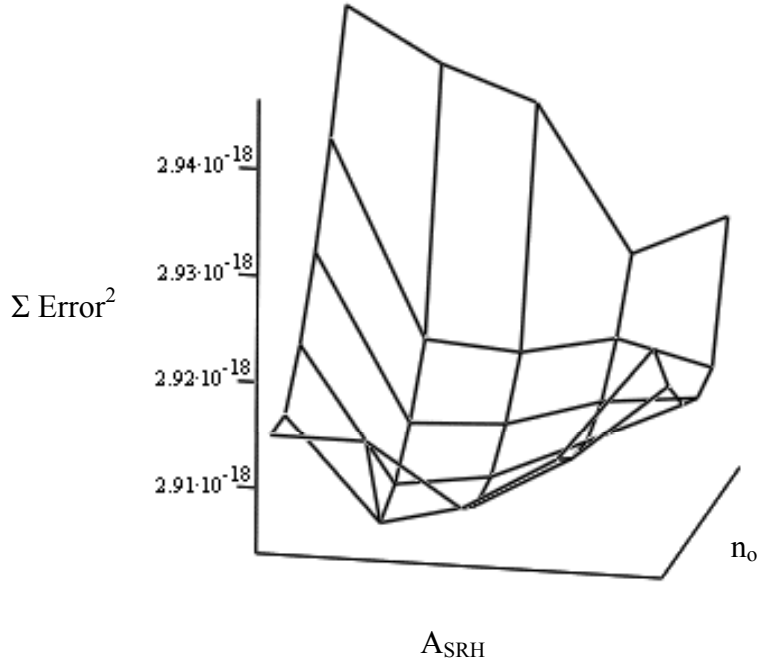


Figure 4.5. Error surface for Sample 91 at 300 mW excitation power resulting from the fit of Eq (4.1) to the experimental data as a function of A_{SRH} and initial carrier density n_0 . Each point represents the minimum error on the B_{rad} and C_{Auger} surface for a given A_{SRH} and n_0 . The minimum point on this surface represents the best fit of the experimental data, yielding all four fitting parameters.

4.1.2. Recombination Coefficient Results

The method describe above was used to fit the data taken from each sample. The decay curve and sample fit for Sample 91 are shown in Figure 4.6. The experiment was performed at various excitation powers. While this causes the initial carrier density to change, the coefficients that describe the recombination processes should remain the same. The Shockley-Read-Hall, radiative, and Auger coefficients calculated for each sample at 300 mW are shown in Table 4.2.

Table 4.2. Experimentally determined recombination coefficients and initial carrier density for each sample at 300 mW.				
Sample	n_0 (cm ⁻³)	A_{SRH}^{-1} (ns)	B_{rad} (cm ³ s ⁻¹)	C_{Auger} (cm ⁻³)
B	$7.0 \pm 0.1 \times 10^{19}$	2 ± 0.5	$2.7 \pm 0.1 \times 10^{-12}$	$3.3 \pm 0.1 \times 10^{-31}$
91	$3.8 \pm 0.1 \times 10^{19}$	82 ± 30	$5.8 \pm 0.5 \times 10^{-11}$	$6.3 \pm 1 \times 10^{-32}$
90	3.5×10^{19}	60	2.9×10^{-11}	5.0×10^{-32}
88	3.6×10^{19}	39	3.5×10^{-11}	6.0×10^{-32}

The error range for Sample 91 resulted from the uncertainty in the absorption coefficient. The data analysis described in the previous section was applied to Sample 91 for both a low and high-end absorption coefficient to study how the uncertainty in the absorption affected the resulting coefficients. The absorption coefficient was known for Sample B, and the largest source of error for this sample is the step size used to vary each of the fitting parameters. The error due to background noise was calculated by determining the standard deviation of the luminescence intensity when the system sampled the same point on the decay curve for thirty iterations. The standard deviation in luminescence intensity was then converted to an error in carrier density. It is assumed that the background noise will affect each point the same. The resulting error due to the background noise was less than 3% of the carrier density, and therefore was considered negligible.

The type II quantum well structures were found to have lower Auger recombination coefficients than the type I structure. This result is in agreement with previous research on InAs that reports type II Auger coefficients an order of magnitude

lower than type I Auger coefficients (Meyer *et al.*, 1998). The reduction in the Auger recombination in this paper is attributed to the removal of the degeneracy between the band-gap energy E_g and the split-off energy gap Δ through band-gap engineering.

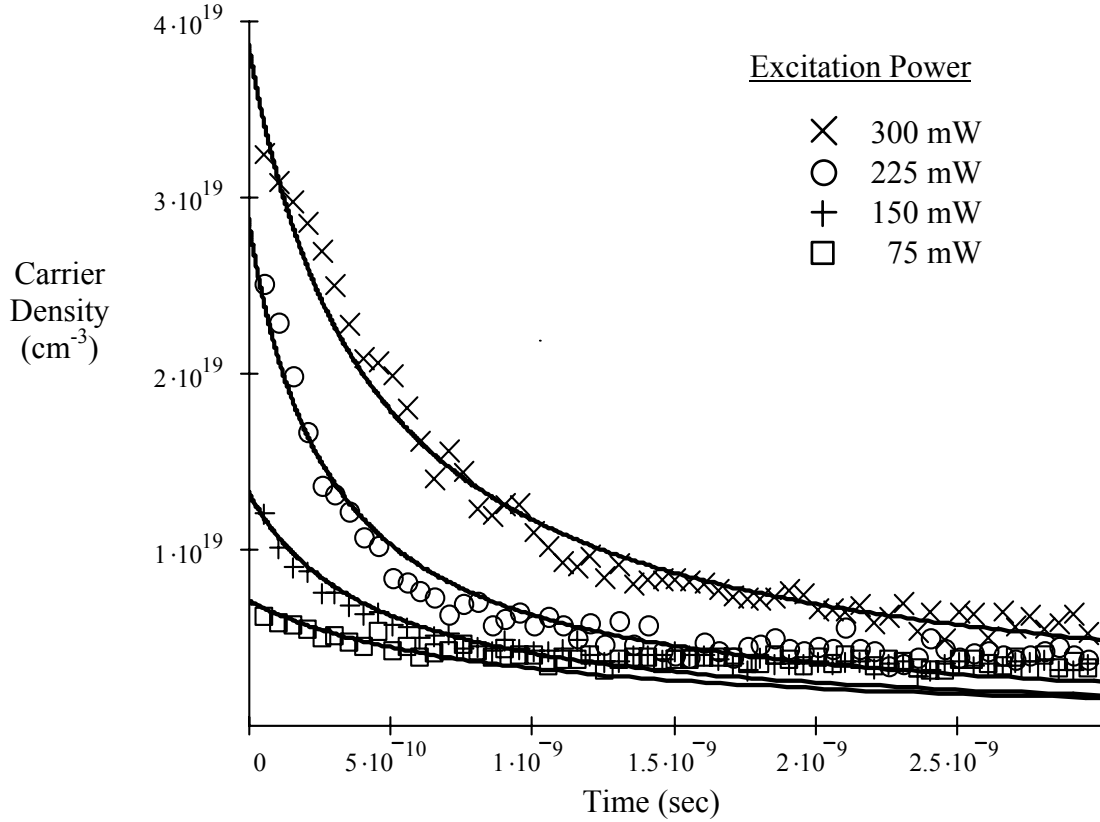


Figure 4.6. Carrier density decay over 3-ns time period for various excitation powers.

4.2. Carrier Relaxation

The recombination coefficients can be used to quantify radiative recombination and nonradiative recombination rates, and thus the efficiency of the device. Another factor influencing device efficiency is carrier relaxation, or how quickly excited carriers cool to the bottom of the quantum well. The time resolved luminescence data was used to study the rise in intensity over the first 50 ps after the excitation pulse. Earlier

reporting indicated that most carriers have relaxed to the band edge states within 15 – 25 ps of excitation (Jang *et al.*, 1996). The rise in luminescence intensity over time corresponds to these carriers cooling from their initial energetic state high in the conduction band to the bottom of the band where they can recombine radiatively.

The luminescence rise was recorded for each sample at various excitation levels, as depicted in Figure 4.7. The rise time was determined from the 10%-90% intensity points on this curve. This convention was previously used by Davis *et al.* to compare carrier relaxation times in a single quantum well structure (Davis *et al.*, 1994).

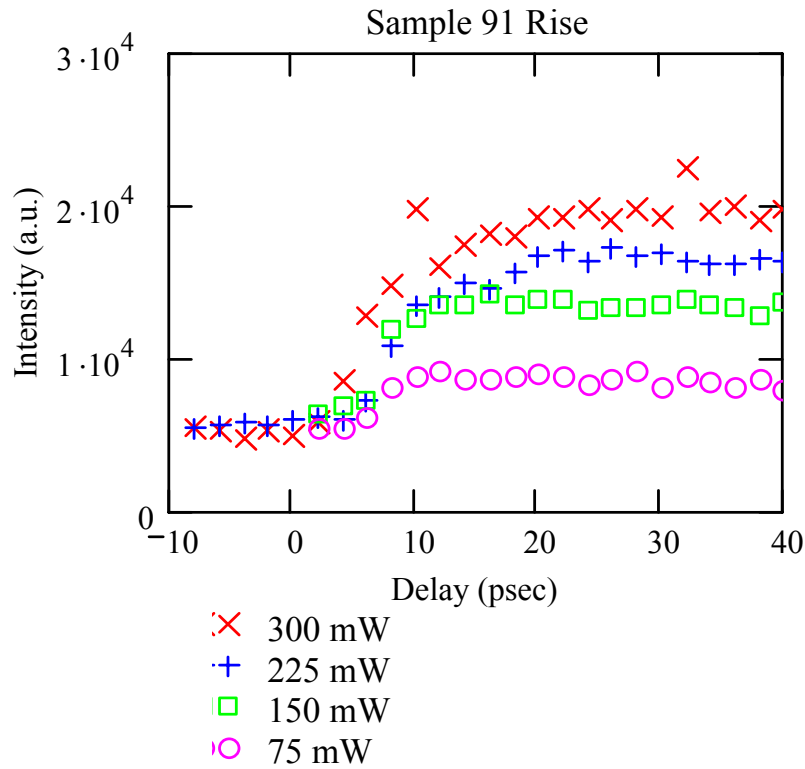


Figure 4.7. Luminescence rise time for Sample 91 at various excitation powers. Data was recorded at 2-ps intervals. Zero on the time scale represents the arrival of the excitation pulse.

The subsequent step in their analysis was to deconvolve the luminescence intensity data with the temporal resolution of the system in order to accurately measure the rise time. Davis *et al.* used a streak camera with 40 ps resolution to obtain the time resolved spectra. This step was omitted in the analysis here because the temporal resolution in this experiment is based on the pump beam pulse width of 122 femtoseconds, which will have no noticeable affect on the recorded data. The resulting rise times for the various samples at different excitation powers is shown in Table 4.3.

Table 4.3. Calculated rise time for each sample at various excitation powers. Rise time is measured from the 10%-90% intensity points.				
Excitation Power (mW)	Rise Time (ps)			
	Sample B	Sample 91	Sample 90	Sample 88
300	20	16	8	5
225	13	12	8	7
150	15	5	6	4
75	-	4	5	-

The rise times for each sample at varying excitation powers were also compared graphically. First, the relationship between carrier density and luminescence shown in Section 4.1.1 was also used here to covert luminescence to carrier density. The data was normalized and fit to an exponential function over the first 40 ps to compare rise times, as seen in Figure 4.8.

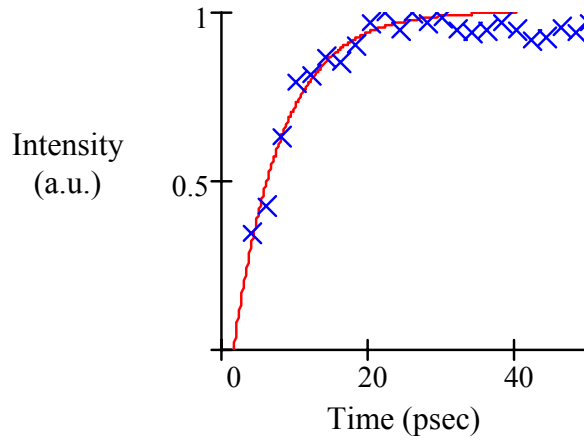


Figure 4.8. Example fit with the function shown to the normalized rise data with $R^2 = 0.97$.

The results indicated that the rise time of the luminescence increases with carrier density, as depicted in Figure 4.9 (a). This goes against a previous report by Boggess, who found a weak indirect dependence of carrier density on rise time (Boggess *et al.*, 2000). One explanation for the difference might involve the density of carriers created in the sample. The initial carrier densities in this experiment are on the order of 10^{19} cm^{-3} . While Boggess did not report the carrier densities involved in the cited work, previous work by the same group typically reported carrier densities on the order of 10^{17} cm^{-3} (Jang and Flatte, 1998; Flatte *et al.*, 1999). At higher carrier densities ($n > 10^{17} \text{ cm}^{-3}$), hot phonon effects become observable (Shah, 1996). A non-equilibrium phonon population arises as carrier cooling creates phonons faster than the phonon energy can be dispersed. The carriers can then reabsorb this phonon energy, thus decreasing the carrier energy loss rate. Yang reports observing this effect in GaAs QW structures (Yang *et al.*,

1985). The carrier relaxation time is slower with increased excitation power, the result of which is seen here in longer rise times.

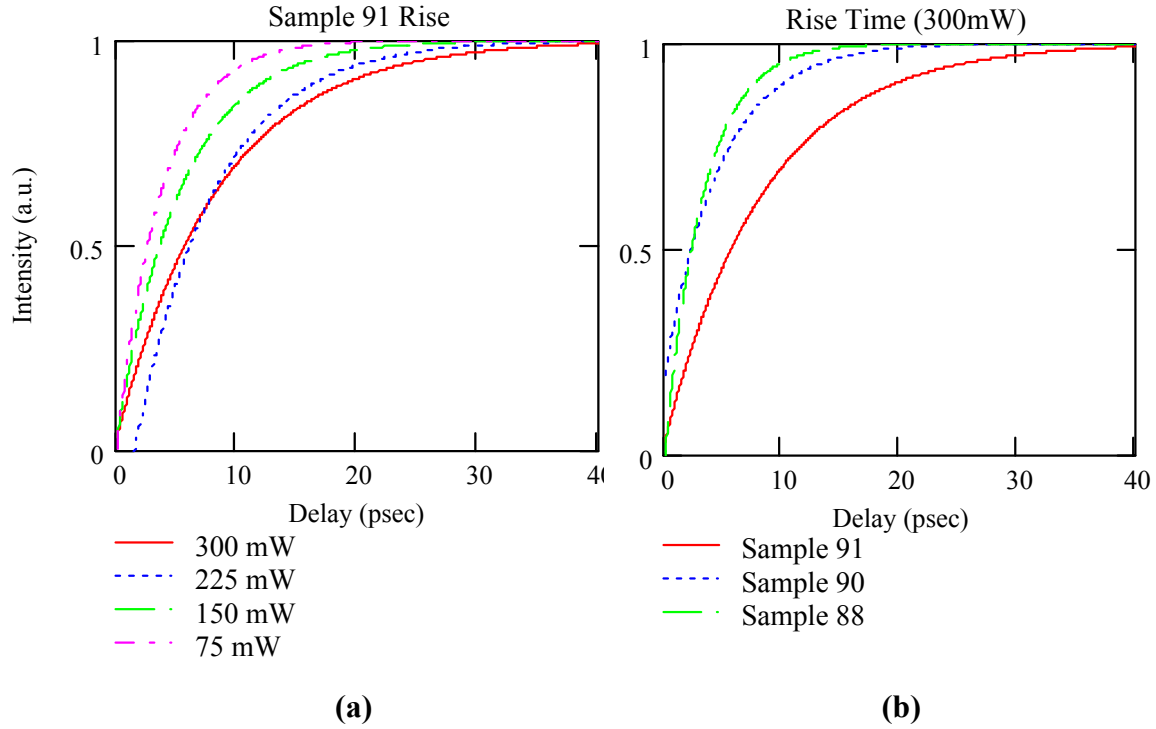


Figure 4.9. Carrier Density rise time for (a) Sample 91 at multiple excitation powers, and (b) for each sample. Rise time increases with carrier density and decreases with well width for the Type II structures.

Figure 4.9 b) shows the rise times of the different samples. The results indicate that rise time will decrease with the quantum well width for the type II structures. This finding is in agreement with previous work on the carrier relaxation in InGaAs/GaAs separate confined heterostructure lasers. Davis *et al.* calculated the multiband coupling coefficient, which represents the wave function overlap integral, for carriers in the quantum well and the continuum of the sample tested (Davis *et al.*, 1994).

The coupling coefficient is directly proportional to the probability of a transition occurring, as given by the Fermi Golden Rule. The probability for a transition between states in a quantum well was found to be much smaller than the probability of making a transition in bulk InGaAs/GaAs (Davis *et al.*, 1994). The result is a bottleneck of carriers at the highest energy state in the quantum well as they wait for the transition to the bottom of the well to occur. The narrower the well, the less likely the transition will occur, and an increase in carrier relaxation time is observed. Narrower quantum wells lasers will have a higher threshold current density and a lower overall efficiency.

4.3. Carrier Temperature

The evolution of the carrier temperature in a semiconductor is closely tied to the rise in the luminescence signal analyzed in the previous section. Electrons initially excited by a laser pulse will give their energy to acoustic and optical phonons, causing the electrons to cool down near the band edge (Shah, 1996:161). At high excitation powers, carrier-carrier interactions dominate, resulting in carrier temperatures higher than the lattice temperature. As time goes on, carrier-optical phonon scattering continues to cool carriers, and the carrier temperature approaches the lattice temperature (Yang, 1985). Auger recombination is dependent on the occupation of energy states within the band structure, which is described by the carrier temperature (Jang and Flatte, 1998).

4.3.1. Carrier Temperature Results

Spectral data was recorded for Sample 91 and Sample B at several times along the luminescence decay curve. Representative spectra for Sample 91 at select time intervals are shown in Figure 4.10. The low energy side of the curve is determined by the band-

gap, as discussed in Chapter 2. Band tailing effects cause luminescence to be observed below the band-gap energy in Figure 4.10. The low energy side of the curve was fit to a Gaussian curve to model line broadening and ensure it was independent of time (Pankove, 1971:45). The empirical parameter in the Gaussian fit has dimensions of energy and describes the density of states, and should remain constant over time.

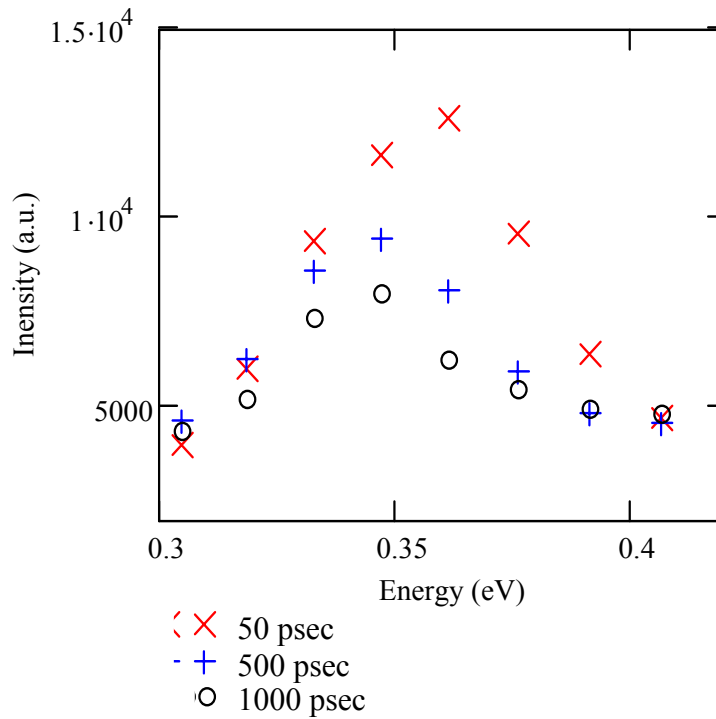


Figure 4.10. Spectral data for Sample 91 at different decay times. The high-energy tail is fit with an exponential function to determine carrier temperature.

The Gaussian fits to the experimental data can be seen in Figure 4.11, and the empirical parameter is shown to vary less than 10% for each curve fit.

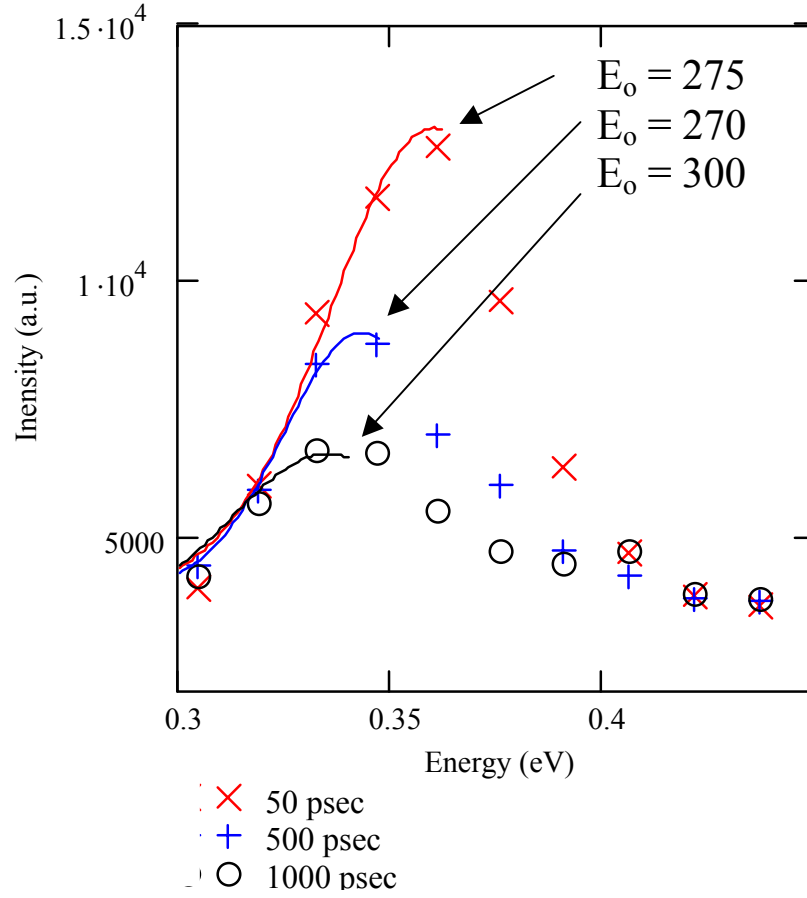


Figure 4.11. Gaussian curve fits to the low energy side of the spectral data. The empirical parameter E_o listed describes the density of states, and was found to vary by less than 10% over the series of spectra.

In non-equilibrium situations, such as photoluminescence, spectral data can be used to calculate carrier temperature. The high-energy portion of the luminescence curve is dictated by the Fermi distribution function described in Chapter 2.

If the carriers have a large amount of energy, as is the case in this experiment, the Fermi function can be approximated by:

$$f(E) = A \cdot e^{\frac{-E}{k \cdot T}}, \quad (4.7)$$

which is the Boltzmann distribution function, where T is the carrier temperature. Eq (4.7) can be used to fit the high-energy side of the luminescence curve, and the carrier temperature at the time the spectra was taken can be determined, as shown in Figure 4.12.

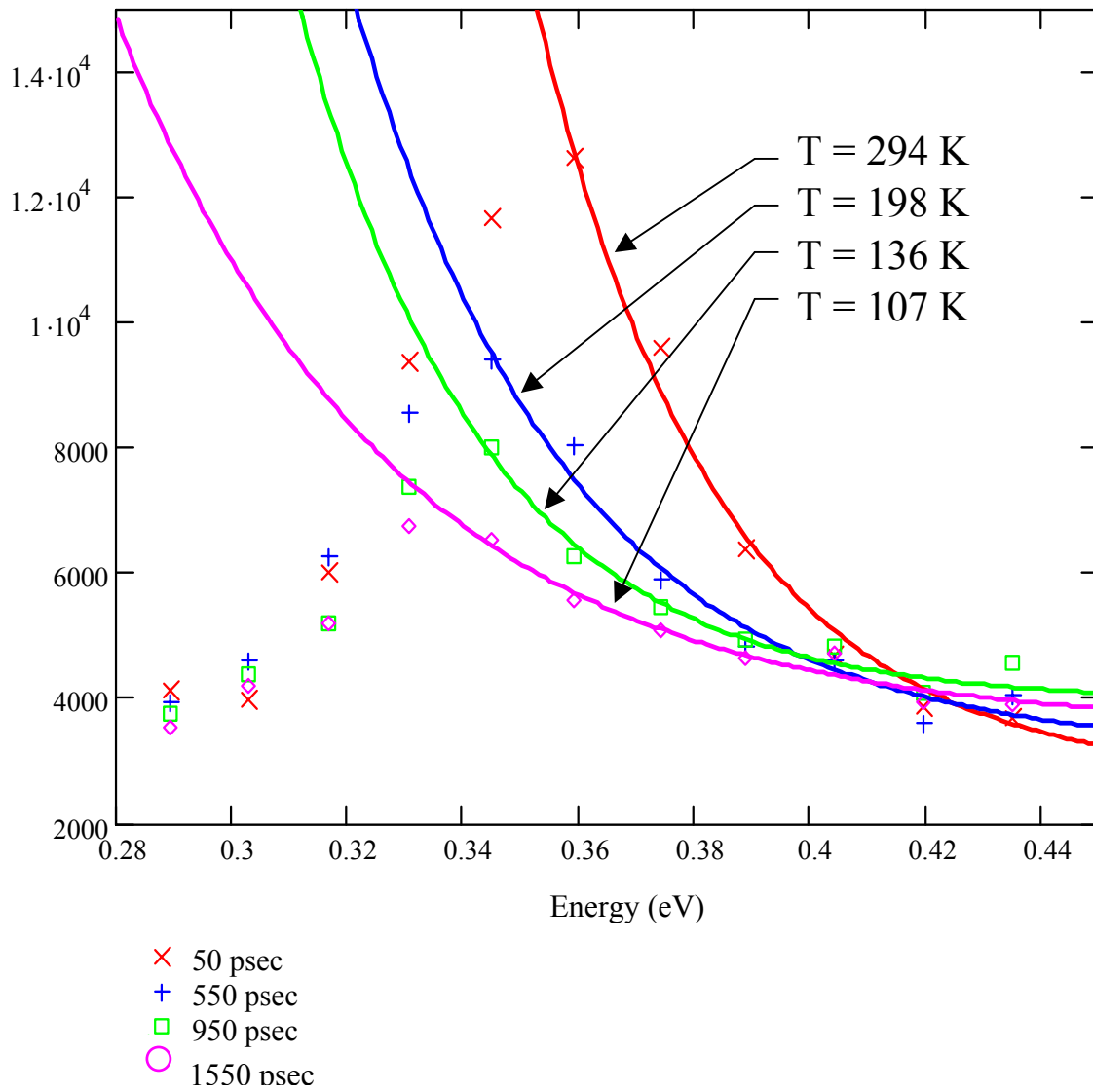


Figure 4.12. Boltzmann distribution curves used to extract carrier temperature shown in figure. Average carrier temperature cools as relax to the band edge and recombine. This method is applied to spectra taken at different times along the luminescence decay

curve to determine how carrier temperature evolves over time. This method was first used in non-equilibrium situations such as this by Linde to measure the change in carrier temperature over time in bulk GaAs (Linde, 1978). Jang *et al.* have reported carrier temperature evolution in mid-IR MQW structures using exponential fitting functions (Jang *et al.*, 1997).

4.3.2. Carrier Temperature Modeling

The time dependence of carrier temperature can be modeled by examining the carrier energy-loss rate with a method described by Shah (Shah, 1996:162-165). The average energy-loss rate per carrier to the lattice can be described by:

$$\frac{dE}{dt} = \frac{E}{\tau_{3D}} \cdot e^{\frac{-E}{k \cdot T}}, \quad (4.8)$$

where E is the longitudinal optical (LO) phonon energy, and T is the carrier temperature (Shah, 1996:163). Optical phonon scattering is dominant at carrier temperatures greater than 40 K, and will be considered the only source of energy loss in this analysis (Yang, 1985). $1/\tau_{3D}$ is the characteristic rate for polar optical phonon scattering and is determined by (Shah, 1996:163):

$$\tau_{3D}^{-1} = \frac{e^2 \cdot \pi \sqrt{2 \cdot m E}}{h^2} \cdot \left(\frac{1}{\epsilon_i} - \frac{1}{\epsilon_s} \right), \quad (4.9)$$

where m is the carrier mass, and ϵ_i and ϵ_s are optical and static dielectric constants. The carrier mass is estimated to be $m = 2.095 \times 10^{-32}$ kg, the effective electron mass in InAs at 300 K (Madelung, 1991). The optical and static dielectric constants for InAs are $12.25 \epsilon_0$ and $15.15 \epsilon_0$, respectively (Madelung, 1991).

The optical phonon scattering rate in Eq (4.9) applies to bulk semiconductors and is related to quantum well structures by:

$$\tau_{2D} = \frac{2}{\pi} \cdot \tau_{3D} \quad (4.10)$$

The optical phonon energy is taken from literature to be approximately 28 meV for mid-IR semiconductors (Jang *et al.*, 1996; Marciniak, 1995). Using these values for an InAs quantum well structure, the longitudinal phonon scattering lifetime is estimated to be 143 fs. The average energy-loss rate by a carrier to the lattice can now be described as a function of temperature, as seen in Figure 4.13.

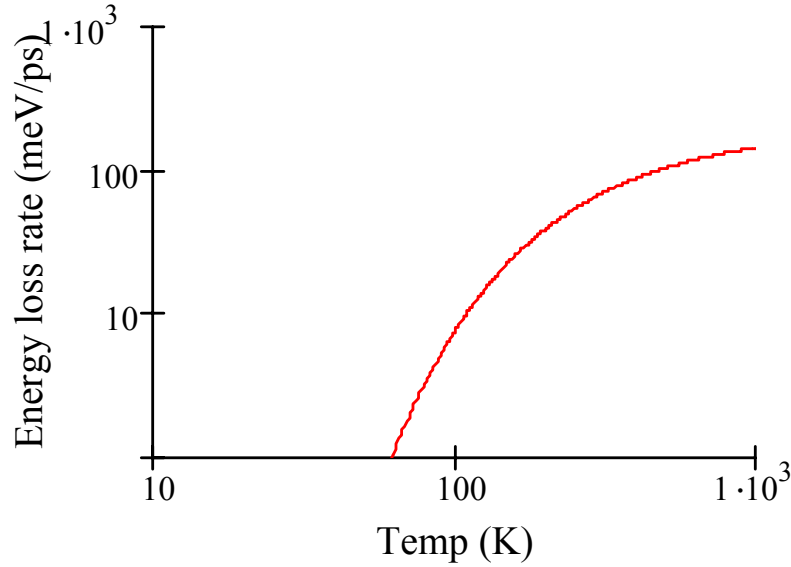


Figure 4.13. Calculated optical phonon energy-loss rate as a function of carrier temperature for InAs. At low temperatures, acoustic phonons dominate resulting in higher loss rates below 40 K, which is not depicted in this figure.

This average energy loss rate can then be equated to the average loss rate of temperature by the following equations (Shah, 1996:165):

$$\frac{\overline{dE}}{dt} = \frac{d}{dt} \bar{E} \quad (4.11)$$

$$t(T_c) = (T_c - T_o) \cdot \frac{-3 \cdot k \cdot T_c}{dE(T_c)},$$

where the average energy $E = 3kT_c$, and T_c , and T_o are the carrier and initial temperatures. Eq (4.11) is numerically inverted to describe the carrier temperature decay as a function of time.

While the model used to determine energy-loss rates in Eq (4.11) is useful in determining how energy is transferred from carriers to phonons, several assumptions were made that will cause experimental results to differ from theory. Two notable assumptions are: 1) phonon occupation remains unaffected by the photoexcitation, and 2) screening affects have been ignored (Shah, 1996:171-173). The danger in making the first assumption is that carriers can reabsorb phonons if the number of phonons is greatly increased by the excitation pulse, causing less energy to be lost than predicted. This is the hot phonon effect discussed in Section 4.2. The second assumption ignores the complex interactions between carriers.

As discussed in Section 2.2, the peak luminescence from an excited sample shifts to lower energies as electrons cool from their excited state. The high-energy side of the spectrum is fit with the exponential in Eq (4.7) to determine carrier temperature as

discussed in the previous section. The temperature results are now plotted in Figure 4.14 along with the theoretical expression for temperature derived in Eq (4.11). A fitting parameter $C = 0.5$ is used to compare the model carrier temperature to experimental results.

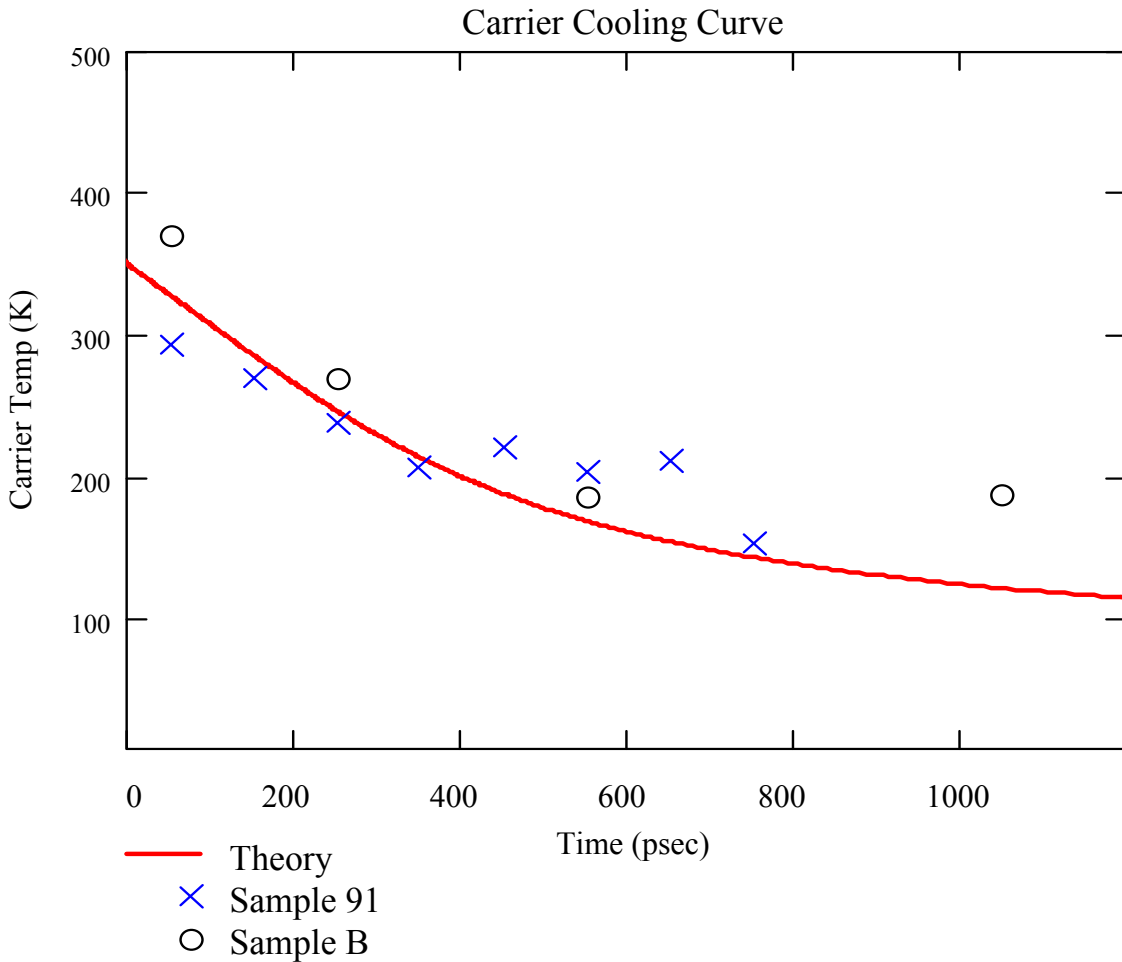


Figure 4.14. Carrier temperature as a function of time for Sample 91 and Sample B. The theoretical model for carrier temperatures in InAs is plotted as a solid line. An initial temperature of 350 K and a fitting parameter $C = 0.5$ was used to fit the data.

This fitting parameter indicates that the carrier loss rate observed is half the rate predicted by the model. Factors that reduce carrier loss rates include the reabsorption of

phonons and carrier screening discussed in the previous section. Fitting parameters between 0.1 – 0.5 have been used to fit previous experimental data to this model for GaAs and InGaAs (Leheny *et al.*, 1979; Kash *et al.*, 1984).

The carrier temperature data in Figure 4.13 indicates that carriers initially cool very rapidly within the first 400 ps, and then the cooling rate begins to taper off. At this point the average carrier energy has fallen far below the characteristic optical phonon energy, which is the prime source of carrier cooling (Jang *et al.*, 1996). The carrier temperatures have not reached the lattice temperature ($T = 77$ K) in the time scale observed. This is likely a result of Auger-induced heating, which contributes energy comparable to the band-gap energy every time an Auger recombination occurs (Jang and Flatte, 1998). Carrier temperatures in Sample B appear to be at least initially higher than Sample 91, which also has a lower Auger coefficient. This reiterates the point that carrier cooling and recombination processes are interrelated events that dictate the efficiency of a semiconductor device.

5. Conclusion

The objective of this research was to study how different semiconductor structures impact carrier recombination and carrier relaxation. The goal is to provide crystal growers feedback on device structures in an effort to increase the overall efficiency of mid-IR semiconductor lasers. This chapter will summarize key findings and make suggestions for future work.

5.1. Summary

Data from the TRPL experiment was used to investigate the recombination coefficients, carrier relaxation, and carrier cooling. The recombination coefficients were calculated by fitting the recombination rate equation to carrier densities over time. Two significant sources of error in determining the coefficients are highlighted. First, the absorption coefficient of the semiconductor leads to the greatest error in computing the initial carrier density. Second, the fitting process used in previous work to calculate the coefficients did not vary every parameter in the recombination rate equation. To find the parameters that best fit the experimental data, each coefficient and the initial condition was varied to minimize the error in the fit. The type I structure was found to have significantly higher Auger coefficients compared to the type II structures.

Analysis of the carrier rise time indicates that the carrier relaxation time will increase at higher excitation powers and with narrower wells. Hot carrier effects cause carriers to reabsorb phonon energy and increase their relaxation time. Narrower wells have a lower probability of downward transitions to the band edge than wider wells, which

causes an increase in relaxation time due to the carrier bottleneck that occurs at the top of the narrow well.

Spectral data from the TRPL experiment was used to extract the carrier temperature over time. It was found that type I structures had higher carrier temperatures than type II structures, which corresponds to the Auger coefficients found for each structure. The Auger process adds energy to the system by promoting a carrier, which is measured as warmer carrier temperatures. These results confirm that type II structures have reduced the impact Auger recombination in mid-IR semiconductor devices.

5.2. Future Work

Future work on this project should be focused in two areas. First, improvements can be made in the analysis to increase the accuracy of the recombination coefficients. Additionally, the TRPL experiment can be converted with some effort to examine mid-IR semiconductor lasers.

As cited earlier, Auger recombination coefficients reported here and elsewhere vary over several orders of magnitude. To accurately compare the efficiency of different structures, the source of these fluctuations must be identified. This research indicates that the absorption coefficient plays a significant role in determining the initial carrier densities. Absorption coefficients should be measured for each sample through ellipsometry or other means to reduce the error in the initial carrier density. In addition, the curve fitting process described in this work could be further automated, which would provide more timely results and allow for further analysis.

One important note in the collection of spectral data is that the upconversion efficiency remained high ($> 90\%$) when performing the experiment over the spectra of Sample 91. This indicates that it may not be necessary to constantly rotate the non-linear crystal in order to record spectral data as suggested in earlier work (Franz, 1997).

The method used in this experiment to collect time-resolved spectra has broader applications than determining carrier temperatures. Laser engineers at Lincoln Laboratory at the Massachusetts Institute of Technology have theorized that unintended modes may exist on a very short time scale in the output of semiconductor lasers. These modes will reduce the gain, and therefore the output power in the desired mode. The TRPL experiment could be converted to examine the output from an optically pumped, mid-IR semiconductor laser to test this theory. The sample laser devices provided by MIT/LL require that the pump beam provide optical confinement in the structure. This requires that the pump beam must be focused on to the sample with a cylindrical lens resulting in a focused spot on the order of 1 mm by 100 microns. The pump beam must also excite the sample from the side rather than from the front as depicted in Figure 3.3. With these exceptions, the TRPL experiment is well suited to investigate laser devices.

Appendix A.

A.1. Crystal Rotation Angle

Appendix A.1. is a program derived from Lt Col Marciniak's Mathematica program deigned to calculate crystal rotation based on PL wavelength.

KTA Rotation Angle

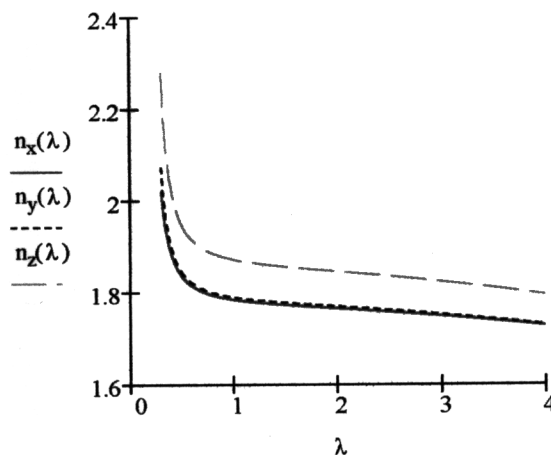
Index ellipsoid for KTA crystal

$$n_x(\lambda) := \sqrt{1.90713 + \frac{1.23522}{1 - \left(\frac{.19692}{\lambda}\right)^2} - .01025 \cdot \lambda^2}$$

$$n_y(\lambda) := \sqrt{2.15912 + \frac{1.00099}{1 - \left(\frac{.21844}{\lambda}\right)^2} - .01096 \cdot \lambda^2}$$

$$n_z(\lambda) := \sqrt{2.14786 + \frac{1.29559}{1 - \left(\frac{.22719}{\lambda}\right)^2} - .01436 \cdot \lambda^2}$$

$\lambda := .3, .31 \dots 4$ λ in μm



Inputs: $\lambda_{PL} := 3.5$ λ in μm

$$\lambda_{\text{Pump}} := .809$$

$$\lambda_{\text{SFG}} := \frac{1}{\frac{1}{\lambda_{PL}} + \frac{1}{\lambda_{\text{Pump}}}} \quad \lambda_{\text{SFG}} = 0.657113$$

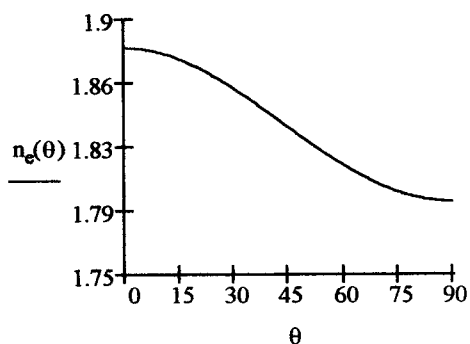
$$n_y(\lambda_{PL}) = 1.740622 \quad n_x(\lambda_{\text{Pump}}) = 1.792606 \quad n_z(\lambda_{\text{Pump}}) = 1.882811 \quad n_y(\lambda_{\text{SFG}}) = 1.811004$$

Determining extraordinary index

$$n_e(\theta_{\text{Pump}}) := \frac{n_x(\lambda_{\text{Pump}}) \cdot n_z(\lambda_{\text{Pump}})}{\sqrt{\left(n_x(\lambda_{\text{Pump}}) \cdot \cos\left(\theta_{\text{Pump}} \cdot \frac{\pi}{180}\right)\right)^2 + \left(n_z(\lambda_{\text{Pump}}) \cdot \sin\left(\theta_{\text{Pump}} \cdot \frac{\pi}{180}\right)\right)^2}}$$

$$n_e(46.49324) = 1.833707$$

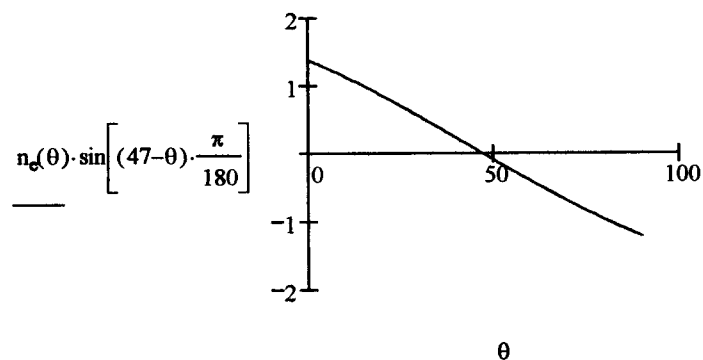
$$\theta := 0..90$$



Snell's law

Crystal cut at 43 degrees

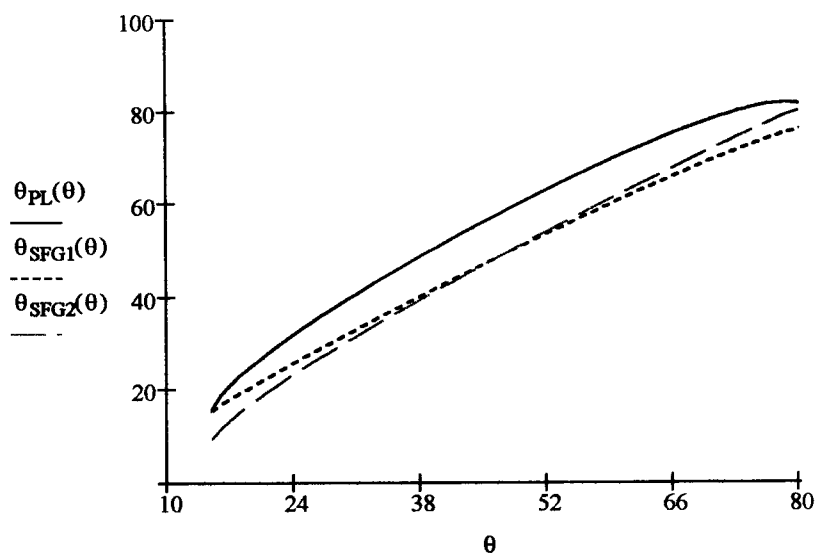
20 degrees between θ_{pl} and θ_{pump}



$$\theta_{PL}(\theta_{Pump}) := \frac{180}{\pi} \cdot \text{asin} \left[\frac{\sin \left[\frac{\pi}{180} \cdot \left[20 - \frac{180}{\pi} \cdot \text{asin} \left[n_e(\theta_{Pump}) \cdot \sin \left(47 - \theta_{Pump} \right) \cdot \frac{\pi}{180} \right] \right] \right]}{n_y(\lambda_{PL})} \right] + 47$$

$$\theta_{SFG1}(\theta_{Pump}) := \frac{180}{\pi} \cdot \text{asin} \left[\left(\frac{n_y(\lambda_{PL}) \cdot \sin \left(\theta_{PL}(\theta_{Pump}) \cdot \frac{\pi}{180} \right)}{\lambda_{PL}} + \frac{n_e(\theta_{Pump}) \cdot \sin \left(\theta_{Pump} \cdot \frac{\pi}{180} \right)}{\lambda_{Pump}} \right) \cdot \frac{\lambda_{SFG}}{n_y(\lambda_{SFG})} \right]$$

$$\theta_{SFG2}(\theta_{Pump}) := \frac{180}{\pi} \cdot \text{acos} \left[\left(\frac{n_y(\lambda_{PL}) \cdot \cos \left(\theta_{PL}(\theta_{Pump}) \cdot \frac{\pi}{180} \right)}{\lambda_{PL}} + \frac{n_e(\theta_{Pump}) \cdot \cos \left(\theta_{Pump} \cdot \frac{\pi}{180} \right)}{\lambda_{Pump}} \right) \cdot \frac{\lambda_{SFG}}{n_y(\lambda_{SFG})} \right]$$



Guess value for intersection

$$\theta_{Pump} := 40$$

Given

$$\theta_{SFG1}(\theta_{Pump}) = \theta_{SFG2}(\theta_{Pump})$$

$$x := \text{Find}(\theta_{Pump})$$

$$x = 46.493242$$

$$\theta_{Pump} := x$$

$$\theta_{PL}(x) = 57.819271$$

$$\theta_{SFG1}(x) = 48.524166$$

$$\theta_{\text{ROT}}(\theta_{\text{Pump}}) := \frac{180}{\pi} \cdot \text{asin} \left[n_y(\lambda_{\text{PL}}) \cdot \sin \left[(\theta_{\text{PL}}(\theta_{\text{Pump}}) - 47) \cdot \frac{\pi}{180} \right] \right]$$

$$\theta_{\text{ROT}}(x) = 19.070727$$

$$\theta_{\text{SFGout}}(\theta_{\text{Pump}}) := \frac{180}{\pi} \cdot \text{asin} \left[n_y(\lambda_{\text{SFG}}) \cdot \sin \left[(\theta_{\text{SFG1}}(\theta_{\text{Pump}}) - 47) \cdot \frac{\pi}{180} \right] \right]$$

$$\theta_{\text{SFGout}}(x) = 2.761013$$

A.2. Finding the Phase Mismatch

Calculate Δk

Phased matched condition

$$\Delta k_x := \frac{n_y(\lambda_{\text{PL}}) \cdot \cos \left(\theta_{\text{PL}}(\theta_{\text{Pump}}) \cdot \frac{\pi}{180} \right)}{\lambda_{\text{PL}}} + \frac{n_e(\theta_{\text{Pump}}) \cdot \cos \left(\theta_{\text{Pump}} \cdot \frac{\pi}{180} \right)}{\lambda_{\text{Pump}}} - \frac{n_y(\lambda_{\text{SFG}}) \cdot \cos \left(\theta_{\text{SFG1}}(\theta_{\text{Pump}}) \cdot \frac{\pi}{180} \right)}{\lambda_{\text{SFG}}}$$

$$\Delta k_z := \frac{n_y(\lambda_{\text{PL}})}{\lambda_{\text{PL}}} \cdot \sin \left(\theta_{\text{PL}}(\theta_{\text{Pump}}) \cdot \frac{\pi}{180} \right) + \frac{n_e(\theta_{\text{Pump}})}{\lambda_{\text{Pump}}} \cdot \sin \left(\theta_{\text{Pump}} \cdot \frac{\pi}{180} \right) - \frac{n_y(\lambda_{\text{SFG}})}{\lambda_{\text{SFG}}} \cdot \sin \left(\theta_{\text{SFG1}}(x) \cdot \frac{\pi}{180} \right)$$

$$\Delta k := \sqrt{\Delta k_x^2 + \Delta k_z^2} \quad \Delta k = 8.836879 \times 10^{-9} \quad \text{Close to zero, as expected}$$

The PL wavelength will be changed to determine Δk

$$\lambda_{\text{PL}} := 3.8$$

$$\theta_{\text{Pump}} := 46.49324$$

$$\lambda_{\text{SFG}} := \frac{1}{\frac{1}{\lambda_{\text{PL}}} + \frac{1}{\lambda_{\text{Pump}}}}$$

$$\lambda_{\text{SFG}} = 0.666999$$

$$\theta_{\text{PL}}(\theta_{\text{Pump}}) := \frac{180}{\pi} \cdot \text{asin} \left[\frac{\sin \left[\frac{\pi}{180} \cdot \left[20 - \frac{180}{\pi} \cdot \text{asin} \left[n_e(\theta_{\text{Pump}}) \cdot \sin \left[(47 - \theta_{\text{Pump}}) \cdot \frac{\pi}{180} \right] \right] \right] \right]}{n_y(\lambda_{\text{PL}})} \right] + 47$$

$$\theta_{\text{SFG1}}(\theta_{\text{Pump}}) := \frac{180}{\pi} \cdot \text{asin} \left[\left(\frac{n_y(\lambda_{\text{PL}}) \cdot \sin\left(\theta_{\text{PL}}(\theta_{\text{Pump}}) \cdot \frac{\pi}{180}\right)}{\lambda_{\text{PL}}} + \frac{n_e(\theta_{\text{Pump}}) \cdot \sin\left(\theta_{\text{Pump}} \cdot \frac{\pi}{180}\right)}{\lambda_{\text{Pump}}} \right) \cdot \frac{\lambda_{\text{SFG}}}{n_y(\lambda_{\text{SFG}})} \right]$$

$$\Delta k_x := \frac{n_y(\lambda_{\text{PL}}) \cdot \cos\left(\theta_{\text{PL}}(\theta_{\text{Pump}}) \cdot \frac{\pi}{180}\right)}{\lambda_{\text{PL}}} + \frac{n_e(\theta_{\text{Pump}}) \cdot \cos\left(\theta_{\text{Pump}} \cdot \frac{\pi}{180}\right)}{\lambda_{\text{Pump}}} - \frac{n_y(\lambda_{\text{SFG}}) \cdot \cos\left(\theta_{\text{SFG1}}(\theta_{\text{Pump}}) \cdot \frac{\pi}{180}\right)}{\lambda_{\text{SFG}}}$$

$$\Delta k_z := \frac{n_y(\lambda_{\text{PL}})}{\lambda_{\text{PL}}} \cdot \sin\left(\theta_{\text{PL}}(\theta_{\text{Pump}}) \cdot \frac{\pi}{180}\right) + \frac{n_e(\theta_{\text{Pump}})}{\lambda_{\text{Pump}}} \cdot \sin\left(\theta_{\text{Pump}} \cdot \frac{\pi}{180}\right) - \frac{n_y(\lambda_{\text{SFG}})}{\lambda_{\text{SFG}}} \cdot \sin\left(\theta_{\text{SFG1}}(x) \cdot \frac{\pi}{180}\right)$$

$$\Delta k := \sqrt{\Delta k_x^2 + \Delta k_z^2}$$

$$\Delta k = 2.968829 \times 10^{-3}$$

Need to determine effective length

Quasi-static interaction length

$$\tau := 122 \cdot 10^{-15}$$

$$n_e := 1.833707 \quad n_o := 1.740662$$

$$c := 3 \cdot 10^8$$

$$v := \left(\frac{c}{n_e}\right)^{-1} - \left(\frac{c}{n_o}\right)^{-1}$$

$$v = 3.1015 \times 10^{-10}$$

$$\Delta\lambda := 10 \cdot 10^{-9} \quad \lambda := 809 \cdot 10^{-9} \quad \Delta\omega := \frac{2 \cdot \pi \cdot c \cdot \Delta\lambda}{\lambda^2}$$

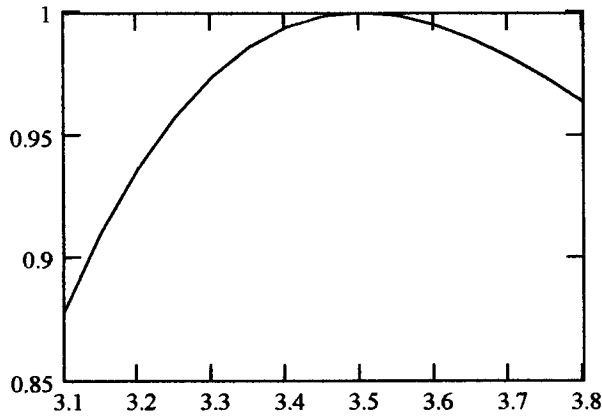
$$L_{\text{qs}} := (v \cdot \Delta\omega)^{-1} \quad L_{\text{qs}} = 1.1195 \times 10^{-4}$$

$$L := 112 \text{ } \mu\text{m}$$

The efficiency equation can now be used

$$\eta := \frac{\sin(L \cdot \Delta k)^2}{(L \cdot \Delta k)^2} \quad \eta = 0.963685$$

The upconversion efficiency is 96.4% of the peak efficiency if upconverting 3.8 μm PL with the crystal tilt optimized for 3.5 μm PL.



Efficiency Curve for λ_{up} near $\lambda_{\text{peak}} = 3.5 \mu\text{m}$

A.3. Carrier Temperature

Constants

$$h := 6.6260755 \cdot 10^{-34}$$

$$k := 1.38065 \cdot 10^{-23}$$

$$q := 1.602177 \cdot 10^{-19}$$

$$E := 28 \cdot 10^{-3} \cdot q \quad \text{Energy of optical phonon taken from Jang 1996}$$

$$\epsilon_0 := 8.854187817 \cdot 10^{-12}$$

$$\epsilon_i := 12.25 \cdot \epsilon_0$$

These are dielectric permittivities taken for InAs

$$\epsilon_s := 15.15 \cdot \epsilon_0$$

$$m := .023 \cdot 9.1093897 \cdot 10^{-31} \quad \text{Electron mass for InAs}$$

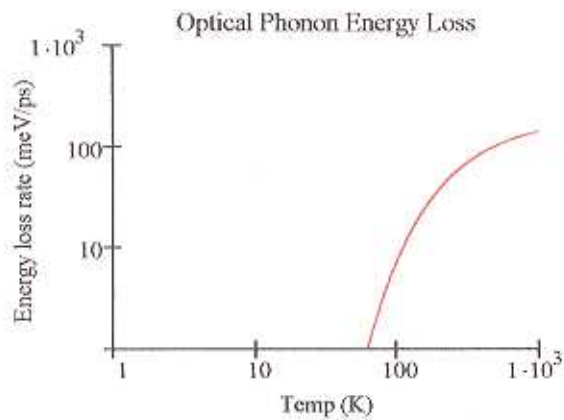
$$\tau_{3D} := \frac{1}{\frac{q^2 \cdot \pi \cdot \sqrt{2 \cdot m \cdot E}}{h^2} \cdot \left(\frac{1}{\epsilon_i} - \frac{1}{\epsilon_s} \right)}$$

$$\tau_{3D} = 2.250005 \times 10^{-13}$$

$$\tau_{2D} := \frac{2}{\pi} \cdot \tau_{3D} \quad \tau_{2D} = 1.432398 \times 10^{-13}$$

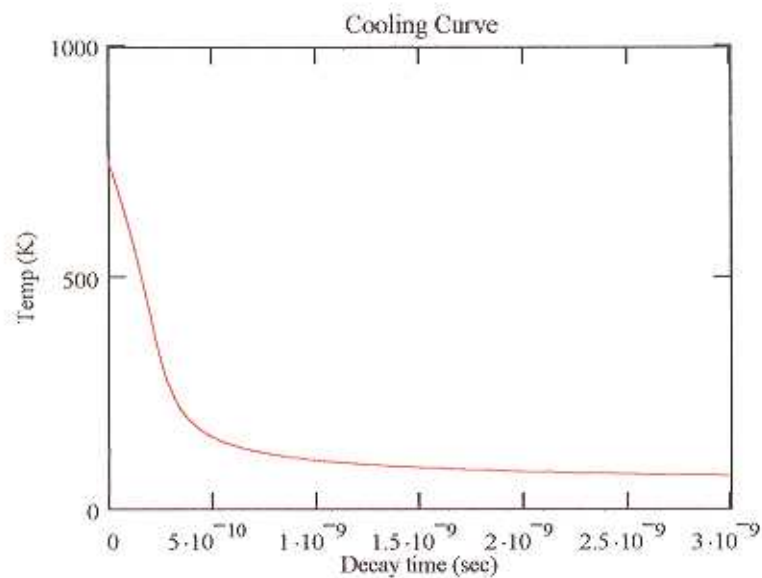
$$dE(T) := \frac{E}{\tau_{2D} \cdot q} \cdot e^{\frac{-E}{k \cdot T}} \quad dE(150) = 2.240455 \times 10^{10} \quad 22 \text{ meV / ps}$$

$$T := 1..1000$$



$$T_0 := 750 \quad C := 0.5 \quad \text{Fitting parameters}$$

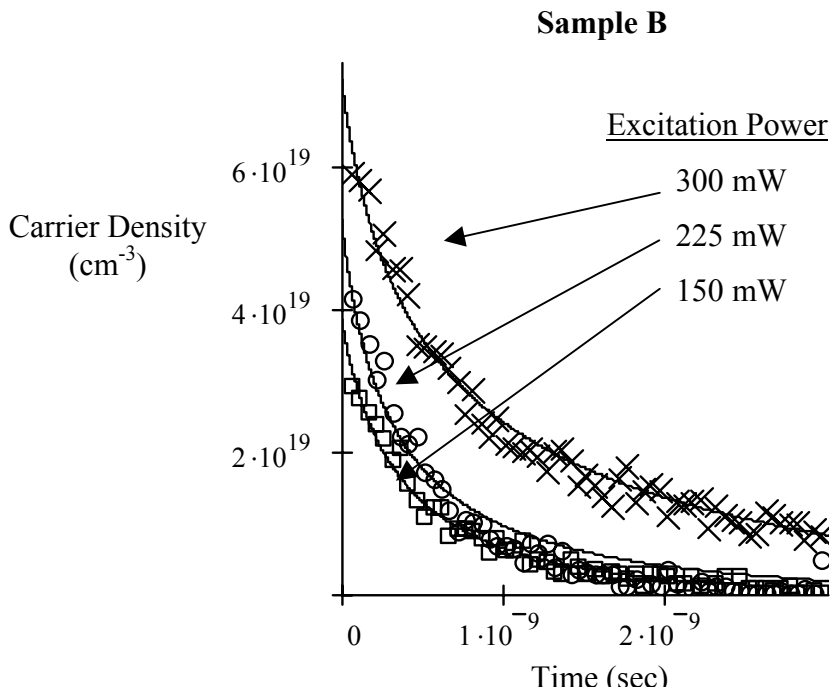
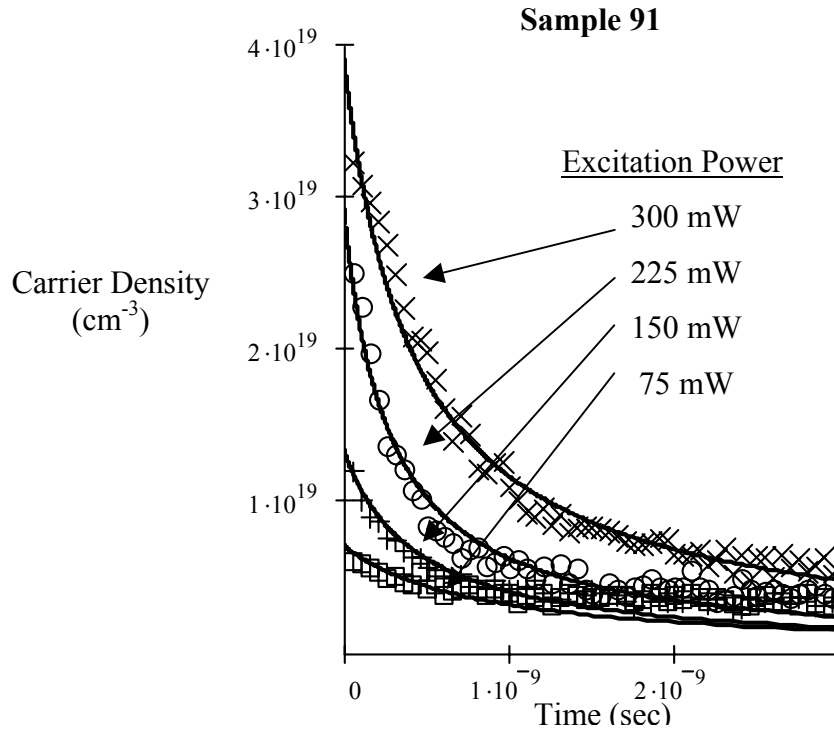
$$t(T_c) := (T_c - T_0) \cdot \frac{-3 \cdot \frac{k}{q} \cdot T_c}{dE(T_c)} \cdot C \quad T_c := 0..1000$$

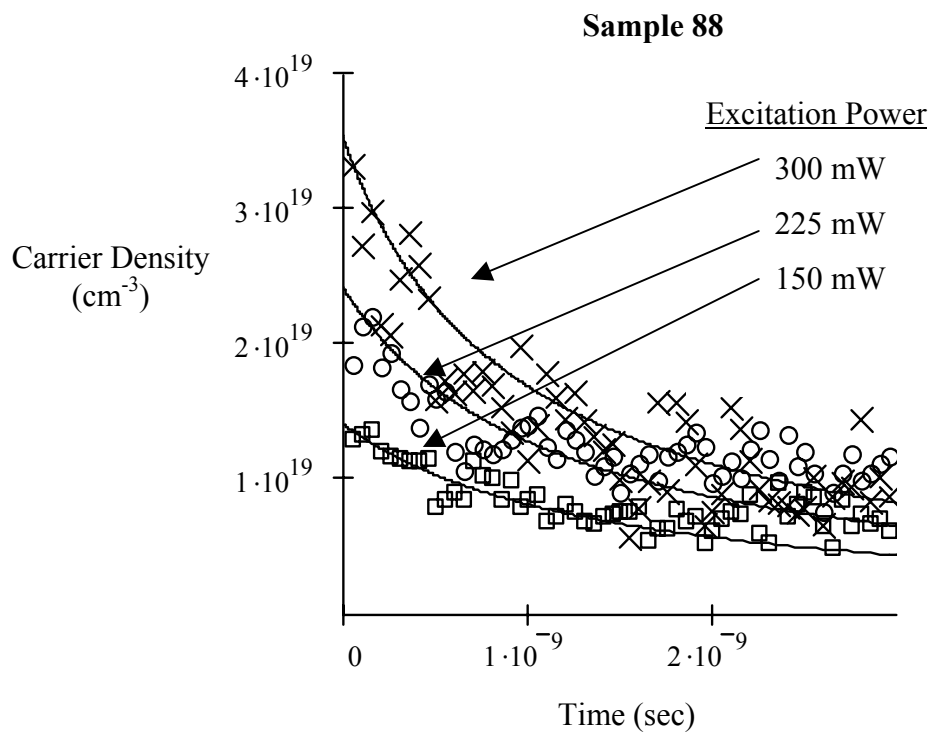
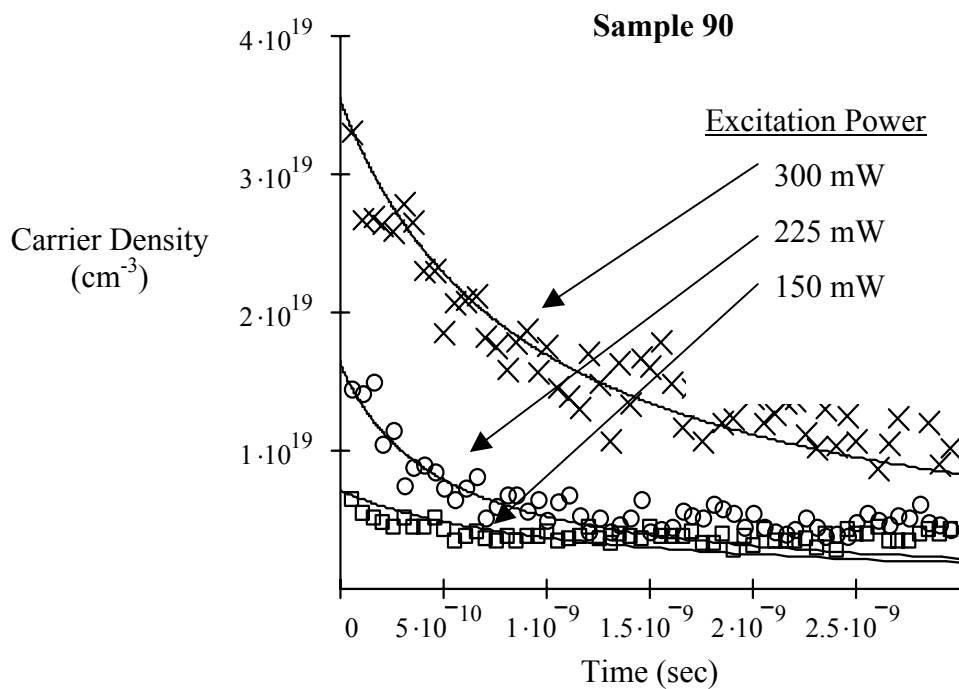


Sample cooling curve for
electrons in InAs with
initial temp = 750 and
C = 0.5

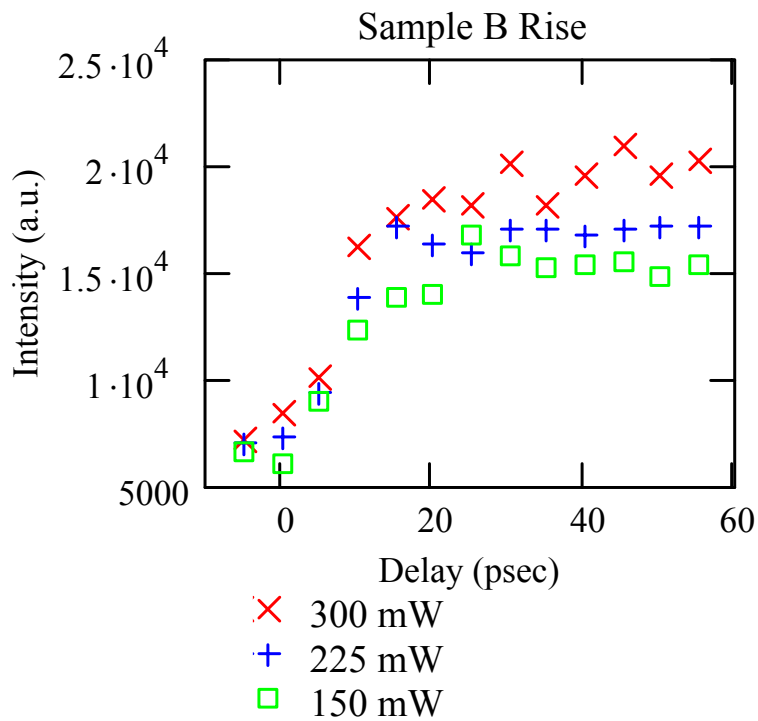
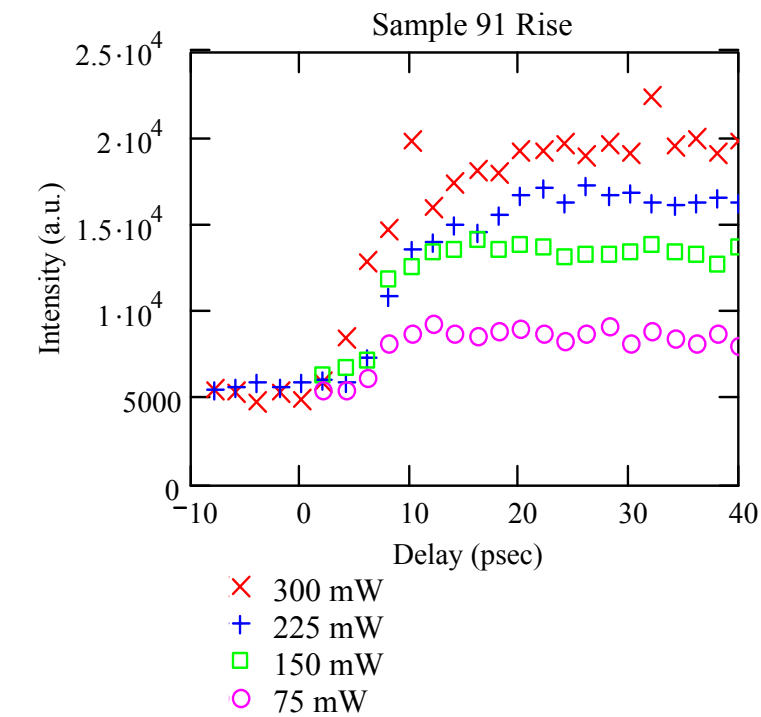
Appendix B

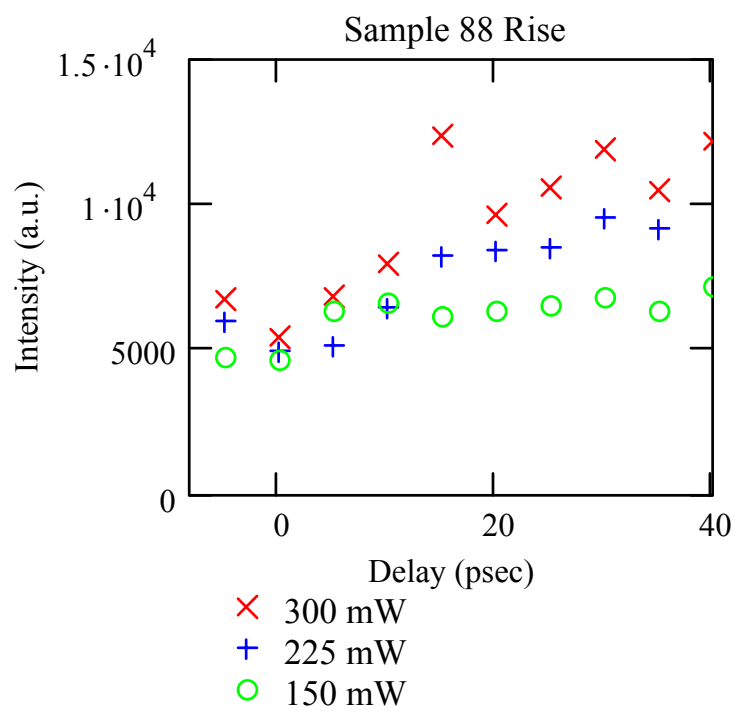
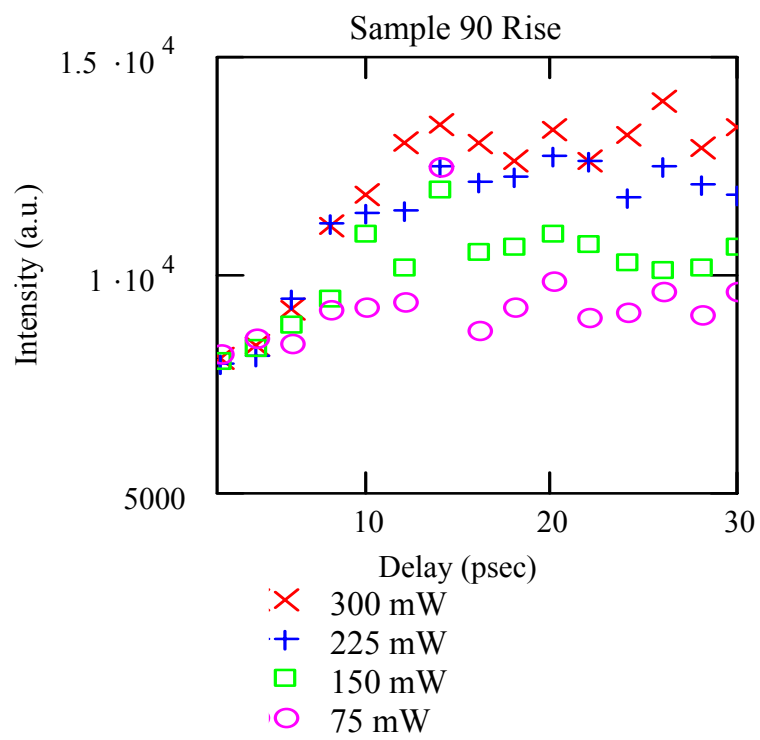
B.1. Decay Curves



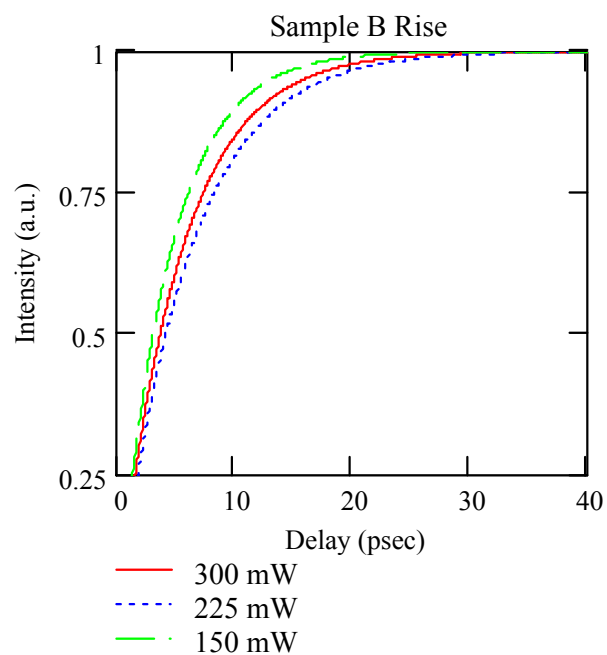
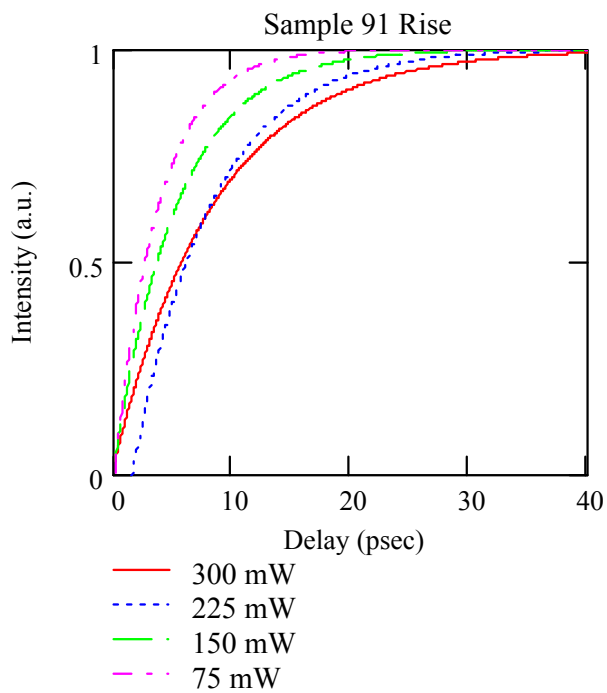
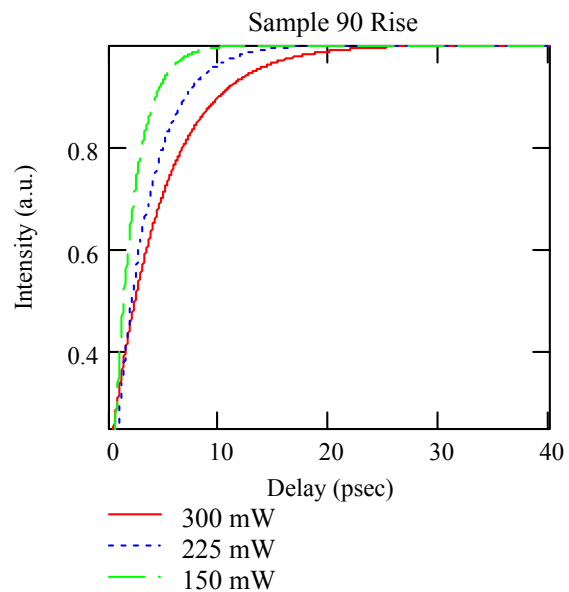
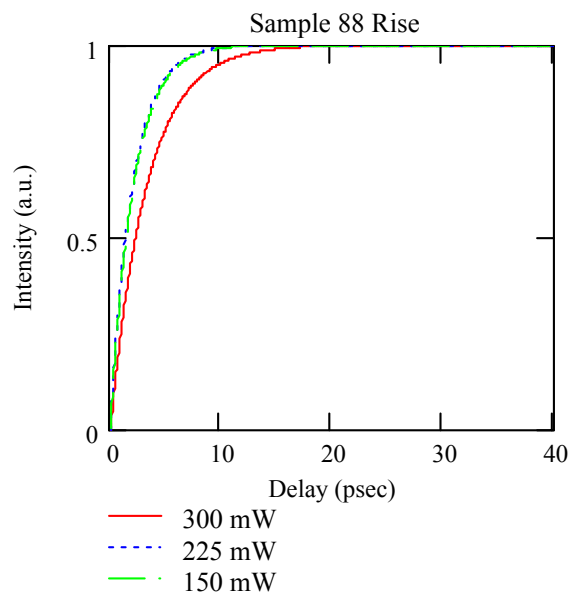


B.2. Raise Time Experimental Data





B.3. Rise Time Curve Fits



Bibliography

Agrawal, A.R. and N.K. Dutta. Semiconductor Lasers (2nd edition). New York: ITP Van Nostrand Reinhold, 1993.

Bhattacharya, P. *Semiconductor Optoelectronic Devices* (2nd edition). New Jersey: Prentice Hall, 1997.

Bhattacharya, P., J. Singh, H.Yoon, X. Zhang, A. Aitken, and Y. Lam. "Tunneling Injection Laser: A new Class of Lasers with Reduced Hot Carrier Effects," *IEEE J. Quantum Electron.* **32**, 1620 (1996).

Boggess, T.F., J.T. Olesberg, and M.E. Flatte. "Ultrafast Optical Measurements of Carrier Dynamics in Antimonide-Based Quantum Wells," *Proceedings of Solid State and Diode Laser Technology Review*. Albuquerque, (5-8 June, 2000).

Boggess, T.F., L. Zhang, and K. Gundogdu. "Application of Ultrafast Mid-Infrared Spectroscopy to the Study of 6.1A-Lattice-Costant Materials," *Proceedings of Solid State and Diode Laser Technology Review*. Albuquerque, (21-24 May, 2001).

Coldren, L.A. and Corzine, S.W. *Diode Laser and Photonic Integrated Circuits*. New York: Wiley-Interscience, 1995.

Cooley, W.T. *Measurement of Ultrafast Carrier Recombination Dynamics in Mid-Infrared Semiconductor Laser Material*, Dissertation, Air Force Institute of Technology, December 1997.

Cooley, W.T., R.L. Hengehold, and Y.K. Yeo. "Recombination dynamics in InAsSb Quantum-well Diode Lasers Measured Using Photoluminescence Upconversion," *Appl. Phys. Lett.* **73**(20) (November 1998).

Davis, L., Y. Lam, Y.C. Chen, J. Singh, and P. Bhattacharya. "Carrier Capture and Relaxation in Narrow Quantum Wells," *IEEE J. Quantum Electron.* **30**, 2560 (1994).

Dmitriev, V.G., G.G. Gurzadyan, and D.N. Nikogosyan, *Handbook of Non-linear Optical Crystals*. Berlin: Springer, 1997.

Fenimore, D.L., K.L. Schepler, U.B. Ramabadran, and S.R. McPherson. "Infrared Corrected Sellmeier Coefficients for Potassium Titanyl Arsenate," *J. Opt. Soc. Am. B*, **12**(5):794 (May 1995).

Flatte, M. E. "Carrier Recombination Rates in Narrow-gap InAs/GaInSb-based Superlattices," *Physical Review B* **59**(8) (February 1999).

- Franz, A.L. *Time-Resolved Photoluminescence Spectra of Mid-Infrared Multiple Quantum Well Laser*, Thesis, Air Force Institute of Technology, (December 1997).
- Goyal, A.K., J. Ochoa, V. Daneu, S.C. Buchter, G.W. Turner, H.K. Choi, J. Walpole, Z.L. Liao, P.J. Foti, M.J. Manfra, T.Y. Fan, and A. Sanchez, "Multispectral Semiconductor Laser System for Infrared Countermeasures," *Proceedings of Solid State and Diode Laser Technology Review*. Albuquerque, (5-8 Jun 2000).
- Haug, A. "Band-to-Band Recombination in Semiconductors," *J. Phys. Chem. Solids* **49**(6):599-605 (1988).
- Hausser, S., G. Fuchs, A. Hangleiter, K. Streubel, and W.T. Tsang. "Auger Recombination in Bulk and Quantum Well InGaAs," *Appl. Phys. Lett.* **56**:913-915 (March 1990).
- Jang, D.J. and M. Flatte. "Temperature Dependence of Auger Recombination in a Multilayer Narrow-band-gap Superlattice," *Physical Review B*. **58**(19) (November 98).
- Jang, D.J., J.T. Olesburg, M. Flatte, Thomas F. Boggess. "Hot Carrier Dynamics in a (GaInSb/InAs)/GaInAlAsSb Superlattice Multiple Quantum Well with Mid-wave Infrared, Subpicosecond Photoluminescence Upconversion," *Appl. Phys. Lett.* **70**(9) (March 1997).
- Kash, K. and J. Shah: *Appl. Phys. Lett.* **45**:401(1984).
- Kent, Brian. "Fundamentals of low observable technology: A Short Course." CD-ROM. AFRL/SNS. 2000.
- Lane, B., D. Wu, A. Rybaltowski, H. Yi, J. Diaz and M. Razeghi. "Compressively Strained Multiple quantum Well InAsSb Lasers emitting at 3.6 μm Grown by Metal-Organic Chemical Vapor Deposition," *Appl. Phys. Lett.* **70**(4) (January 1997).
- Lambeth, B.S. "NATO'S Air War For Kosovo: A Strategic and Operational Assessment." Excerpt from unpublished article. <http://www.rand.org/publications/MR/MR1365/MR1365.ch6.pdf>. 2001.
- Leheny, R.F., J. Shah, R.L. Fork, C.V. Shank, and A. Migus: *Solid State Commun.* **18**:487 (1976).
- Lindle, D. and R. Lambrich. "Direct Measurement of Hot-Electron Relaxation by Picosecond Spectroscopy," *Physical Review Letters* **42**(16) (April 1979).
- Lindle, J.R., J.R. Meyer, C.A. Hoffman, and F.J. Bartoli. "Auger lifetime in InAs, InAsSb, and InAsSb-InAlAsSb Quantum wells," *Appl. Phys. Lett.* **67**(21) (November 1995).

Madelung, O. *Data in Science and Technology: Semiconductors, Group IV Elements and III-V Compounds*. Berlin: Springer, 1991.

Mahr, H. and M.D. Hirsch. "An Optical Up-Conversion Light Gate with Picosecond Resolution," *Optical Communications* **13**(2):96 (February 1975).

Marciniak, M.A. *Optical Characterization of MBE-Grown InAs_{1-x}Sb_x Semiconductors on GaSb Substrate*, Dissertation, Air Force Institute of Technology, (August 1995).

McKay, M. *Time-Resolved Photoluminescence of InAs/GaInSb Quantum Well Lasers*, Thesis, Air Force Institute of Technology, (May 2000).

McKelvey, J.P. *Solid state Physics for Engineering and Material Sciences*. Florida: Krieger Publishing, 1993.

Meyer, J.R., C.L. Felix, W.W. Bewley, I. Vurgaftman, E.H. Aifer, L.J. Lindle, C.A. Hoffman, M.J. Yang, B.R. Bennett, and B.V. Shanabrook. "Auger coefficients in type II InAs/GaInSb Quantum Wells," *Appl. Phys. Lett.* **73**(20):2857-2859 (November 1998).

Pankove, J.I. *Optical Processes in Semiconductors*. New York: Dover, 1971.

Saleh, B.E.A. and M.C. Teich. *Fundamentals of Photonics*. New York: Wiley-Interscience, 1991.

Sanders Press Release. "New Laser Portends Breakthrough In Directable IRCM Systems." Excerpt from unpublished article. http://www.iewns.na.baesystems.com/business/00_news/sa1827.htm. 28 March 2000.

Sawyer, Thomas. "CLIRCM: Next Generation Counter to the Deadly IR Missile." Excerpt from unpublished article. <http://www.davidbonior.house.gov/pitts/initiatives/ew/010724ew-brief-10.htm>. 24 July 2000.

Sermage, B., D.S. Chemla, D. Sivco, and A.Y. Cho. "Comparison of Auger Recombination in GaInAs-AlInAs Multiple Quantum Well Structures and in Bulk GaInAs," *Appl. Phys. Lett.*, **50**(19):1307-1309 (May 1997).

Shah, Jagdeep. *Ultrafast Spectroscopy of Semiconductors and Semiconductor Nanostructures*. Berlin: Springer, 1996.

Shah, Jagdeep. "Ultrafast Luminescence Spectroscopy Using Sum Frequency Generation," *IEEE Journal of Quantum Electronics*, **QE-24**(2):276-288 (February 1988).

Snow, P.A., P. Maly, D.J. Westland, and J.F. Ryan. "Picosecond Photoluminescence Measurements of Hot Carrier Relaxation and Auger Recombination in GaSb," *Solid-State Electronics* **32**(12):1485-1489 (1989).

Taylor, William. "Laser Infrared Flyout Experiment Affordability Measures." Excerpt from unpublished article. <http://afrlhorizons.com/Briefs/Mar01/SN0004.html>. March 2001.

Turner, G.W., H. K. Choi, and H.Q. Le. "Growth of InAsSb Quantum Wells for Long-wavelength lasers," *J. Vac. Sci. Technol. B* **13**(2) (Mar/Apr 1995).

Verdeyen, J.T. *Laser Electronics* (3rd edition). New Jersey: Prentice Hall, 1995.

Weeks, David. Private Communication, (2002).

Yang, C.H., J.M. Carlson-Swindle, and S.A. Lyon. "Hot electron Relaxation in GaAs Quantum Wells," *Phy. Rev. Lett.* 55(21) (November 1985).

Yarvi, A. and P. Yeh. *Optical Waves in Crystals*. New York: Wiley Interscience, 1984.

Zhang, L., Thomas F. Boggess, D. G. Deppe, D. L. Huffaker, O. B. Shchekin, and C. Cao. "Dynamic Response of 1.3- μ m-Wavelength InGaAs/GaAs Quantum Dots," *Appl. Phys. Lett.* **76**(10) (March 2000).

REPORT DOCUMENTATION PAGE

Form Approved
OMB No. 0704-0188

Public reporting burden for this collection of information is estimated to average 1 hour per response, including the time for reviewing instructions, searching existing data sources, gathering and maintaining the data needed, and completing and reviewing the collection of information. Send comments regarding this burden estimate or any other aspect of this collection of information, including suggestions for reducing this burden, to Washington Headquarters Services, Directorate for Information Operations and Reports, 1215 Jefferson Davis Highway, Suite 1204, Arlington, VA 22202-4302, and to the Office of Management and Budget, Paperwork Reduction Project (0704-0188), Washington, DC 20503.

1. AGENCY USE ONLY (Leave blank)		2. REPORT DATE 20020304	3. REPORT TYPE AND DATES COVERED Master's Thesis	
4. TITLE AND SUBTITLE CARRIER DYNAMICS IN MID-INFRARED QUANTUM WELL LASERS USING TIME-RESOLVED PHOTOLUMINESCENCE			5. FUNDING NUMBERS	
6. AUTHOR(S) Gorski, Steven M., Captain, USAF				
7. PERFORMING ORGANIZATION NAME(S) AND ADDRESS(ES) Air Force Institute of Technology Graduate School of Engineering and Technology (AFIT/EN) 2950 P. Street, Building 640 WPAFB, OH 45433-7765			8. PERFORMING ORGANIZATION REPORT NUMBER AFIT/GAP/ENP/02M-01	
9. SPONSORING/MONITORING AGENCY NAME(S) AND ADDRESS(ES) Air Force Research Laboratory Directed Energy Directorate Attn: Ms. Sylvia Dorato Kirtland AFB, NM 87117			10. SPONSORING/MONITORING AGENCY REPORT NUMBER	
11. SUPPLEMENTARY NOTES				
12a. DISTRIBUTION AVAILABILITY STATEMENT APPROVED FOR PUBLIC RELEASE: DISTRIBUTION UNLIMITED			12b. DISTRIBUTION CODE	
13. ABSTRACT (Maximum 200 words) Research in mid-infrared laser technology has uncovered numerous applications for commercial and government use. A limiting factor for mid-infrared semiconductors is nonradiative recombination, which is a process that produces excess heat without emitting a photon. Nonradiative recombination mechanisms occur over a short time period and difficult to measure. Growth methods have significantly reduced the nonradiative recombination in some materials. The objective of this research is to further the understanding of how quantum well structures impact carrier recombination. InAsSb/InAlAsSb and InAs/GaInSb quantum well structures were studied with time-resolved photoluminescence utilizing upconversion, a non-linear wave mixing technique. This research reports Shockley-Read-Hall, radiative, and Auger recombination coefficients at 77 K. The luminescence rise times of type I and type II structures are also compared. The number of states available within the quantum well was found to dictate how quickly carriers were able to recombine radiatively. Finally, spectral data was taken to examine the spectral decay of the luminescence. Carrier temperatures were extracted from the spectral data. Type I structures were found to have hotter carrier temperatures and higher Auger coefficients than type II structures.				
14. SUBJECT TERMS Time resolved photoluminescence, Sum frequency generation, upconversion, quantum well lasers, Gallium Indium Antimonide, Indium Arsenide, Indium Aluminum Arsenide Antimonide, carrier relaxation time, photoluminescence spectra, Auger recombination			15. NUMBER OF PAGES 80	
			16. PRICE CODE	
17. SECURITY CLASSIFICATION OF REPORT U	18. SECURITY CLASSIFICATION OF THIS PAGE U	19. SECURITY CLASSIFICATION OF ABSTRACT U	20. LIMITATION OF ABSTRACT UU	